JGR Solid Earth

RESEARCH ARTICLE
10.1029/2021JB022584

Reaction-Induced Mantle Weakening at High-Pressure Conditions: An Example From Garnet Pyroxenites of Ulten Zone (Eastern Alps, N Italy)

L. Pellegrino[1], L. Menegon[2], S. Zanchetta[1], F. Langenhorst[3,4], K. Pollok[3], S. Tumiati[5], and N. Malaspina[1]

[1]Department of Earth and Environmental Sciences, University of Milano-Bicocca, Milano, Italy, [2]Department of Geosciences, The Njord Centre, University of Oslo, Oslo, Norway, [3]Institute of Geosciences, Friedrich Schiller University Jena, Jena, Germany, [4]School of Ocean and Earth Science and Technology, Hawai'i Institute of Geophysics and Planetology, University of Hawai'i at Manoa, Honolulu, USA, [5]Department of Earth Sciences, University of Milano, Milano, Italy

Key Points:

- In websterites of Ulten zone, pyroxenes switch from dislocation to diffusion-creep-dominated deformation
- The transition in deformation mechanism took place during the prograde re-equilibration of websterites in the garnet stability field
- This results in the rheological weakening of websterites during the corner flow of the lithospheric mantle induced by the slab subduction

Supporting Information:

Supporting Information may be found in the online version of this article.

Correspondence to:

L. Pellegrino and N. Malaspina,
luca.pellegrino@unimib.it;
nadia.malaspina@unimib.it

Citation:

Pellegrino, L., Menegon, L., Zanchetta, S., Langenhorst, F., Pollok, K., Tumiati, S., & Malaspina, N. (2021). Reaction-induced mantle weakening at high-pressure conditions: An example from garnet pyroxenites of Ulten Zone (Eastern Alps, N Italy). *Journal of Geophysical Research: Solid Earth*, *126*, e2021JB022584. https://doi.org/10.1029/2021JB022584

Received 10 JUN 2021
Accepted 21 NOV 2021

Abstract Peridotites of Ulten Zone (Eastern Alps, N Italy) show a transition from coarse protogranular spinel lherzolites to fine-grained amphibole + garnet peridotites, recorded by the crystallization of garnet coronas around spinel. Pyroxenite veins, transposed along the peridotite foliation, show a similar metamorphic evolution from coarse-grained (garnet-free) websterites to fine-grained garnet websterites. In both peridotites and websterites, garnet previously exsolved from porphyroclastic high-temperature pyroxenes and later crystallized along the foliation. This evolution has been interpreted to reflect cooling and pressure increase of websterites and host peridotites from spinel- to garnet-facies conditions. Microstructures and crystallographic orientation data indicate that the re-equilibration of garnet websterites in the garnet stability field occurred during deformation. Porphyroclastic pyroxenes have been interpreted to deform by dislocation glide and creep. In particular, TEM observations indicate the activation of the (100)[010] slip system in orthopyroxene. Core-and-mantle microstructures also suggest that dislocation creep was aided by subgrain rotation recrystallization, leading to the formation of neoblastic pyroxenes. These recrystallized grains deformed by diffusion-accommodated grain boundary sliding, as indicated by the occurrence of quadruple junctions and straight, aligned grain boundaries. The transition from dislocation creep to diffusion creep in websterites was accompanied by the crystallization of garnet along foliation, which triggered the pinning of the recrystallized matrix and stabilized the fine-grained microtexture for diffusion creep, promoting rheological weakening. Garnet websterites of Ulten Zone thus offer a unique opportunity to investigate the effects of reaction softening during the corner flow in the supra-subduction lithospheric mantle induced by the descending slab.

Plain Language Summary When tectonic plates converge, one plate slides beneath the other plate descending into the Earth's mantle. During this process (the so-called subduction), rocks forming the Earth's mantle, such as peridotites and pyroxenites, can be dragged to great depths and later transported back to the surface by a combination of two processes known as corner flow and exhumation. Rocks that experienced this journey are now exposed at the surface only in few mountain belts in the world (such as the European Alps) and represent natural laboratories to study the processes that occur at great depths in the Earth's mantle. In this study, we reconstruct the metamorphic and deformation evolution of pyroxenites of the Ulten Zone (Eastern Alps, N Italy). Minerals in pyroxenites deformed through different deformation processes, including dislocation creep and diffusion creep mechanisms. Our data indicate that minerals within pyroxenites record a transition in the deformation mechanism from dislocation to diffusion creep. This switch of the deformation mechanism was responsible for a significant rheological weakening of pyroxenites, suggesting that pyroxenites can play a major role in the processes that control the deformational behavior of the Earth's mantle.

1. Introduction

The deformational behavior of the upper mantle in response to the forces in the Earth's interior depends on several factors, including pressure, temperature, deviatoric stress, mineralogy, presence of fluids and/or melts, and the grain size of the deforming mantle rocks (e.g., Bürgmann & Dresen, 2008 and reference therein). Studies on both naturally and experimentally deformed mantle rocks indicate that most of the plastic deformation of the upper mantle is accommodated by grain size insensitive (GSI) deformation mechanisms, e.g., dislocation creep

(Bai and Kohlstedt, 1992; Demouchy et al., 2009; Doukhan et al., 1984; Durham and Goetze, 1977; Durham et al., 1977; Jung et al., 2006).

In particular, at upper mantle conditions, mantle minerals (e.g., olivine and pyroxenes) are expected to deform through dislocation glide and creep on specific crystallographic planes and directions (slip systems), resulting in the formation of a crystallographic preferred orientation (CPO), which is a function of the available slip systems and the strain regime. However, field-based microstructural studies on mantle shear zones suggest that a significant part of the deformation may also be accommodated by grain-size sensitive (GSS) creep processes, e.g., diffusion creep and grain boundary sliding (Warren & Hirth, 2006; Skemer et al., 2010; Kaczmarek & Tommasi, 2011; Vauchez et al., 2012). These studies also highlight that the grain size within shear zones is typically smaller than the grain size of the host rocks (e.g., Drury et al., 1991; White et al., 1980), suggesting that dynamic recrystallization cooperates with creep mechanisms during deformation and strain localization. Grain-size reduction by dynamic recrystallization is believed to be principally responsible for the transition in the deformation mechanism from dislocation creep to diffusion creep processes (Handy, 1989; Jaroslow et al., 1996; Skemer et al., 2010; Toy et al., 2010) and thus of the consequent rheological weakening (Hansen et al., 2011; Hirth & Kohlstedt, 2003; Rutter & Brodie, 1988). However, De Bresser et al. (2001) demonstrated that grain-size reduction may not be sufficient to cause a permanent transition from dislocation to diffusion creep because minerals tend to grow with time. Nevertheless, syn-deformational metamorphic reactions are able to inhibit grain growth (e.g. Newman et al., 1999), since the crystallization of new minerals (i.e., the so-called second phases) can trigger the pinning of the recrystallized matrix, preventing grain coarsening and thus stabilizing the fine-grained microtexture for diffusion creep (Linckens et al., 2011; Précigout et al., 2007; Warren and Hirth, 2006).

Microstructural studies on natural rocks indicate that syn-deformational metamorphic reactions such as the breakdown of mantle aluminous phases (plagioclase, spinel, or garnet) can promote rheological weakening in the upper mantle (e.g., Furusho & Kanagawa, 1999; Hidas et al., 2013; Kaczmarek & Tommasi, 2011; Newman et al., 1999; Toy et al., 2010). These studies demonstrate that syn-deformational breakdown reactions generate fine-grained reaction products in which deformation can be localized. This process triggers the transition from dislocation to diffusion creep, thus facilitating rheological weakening. Experimental studies also indicate that the transition from plagioclase to spinel and garnet facies in the mantle is strongly affected by the whole-rock concentration of major elements such as Al_2O_3, Cr_2O_3, CaO, and Na_2O (Adam et al., 1992; Borghini et al., 2010; Fumagalli & Poli, 2005; Irving, 1974; Schmädicke, 2000; Ziberna et al., 2013). In particular, these studies pointed out that the breakdown of these aluminous minerals occurs at different pressures in pyroxene-rich mantle rocks compared to peridotites, therefore suggesting that the locus and the degree of deformation in the upper mantle may also be controlled by the occurrence and the distribution of compositional heterogeneities such as pyroxenites l.s..

The Ulten zone (Tonale Nappe, Eastern Alps, N Italy) is one of the best examples of metamorphic terrane where peridotites from the supra-subduction mantle record the transition from spinel- to garnet-facies conditions resulting from the corner flow triggered by the subduction of an old continental crust (Godard et al., 1996; Nimis & Morten, 2000; Scambelluri et al., 2010; Tumiati et al., 2003). These peridotites are veined by numerous websterites, which record the same textural/metamorphic evolution of the host rocks (Gebauer & Grünenfelder, 1978; Nimis & Morten 2000). We will show that these websterites underwent a textural transformation from coarse-grained (garnet-free) to finer-grained (garnet-bearing) websterites reflecting the cooling and pressure increase from spinel- to garnet-facies conditions, also recorded by the host peridotites, during the mantle corner flow. In particular, microstructures indicate that the transition from garnet-free to garnet-facies conditions occurred in a deformation regime and was accompanied by a reaction-induced reduction of the grain size, which triggered the switch of the deformation mechanism from dislocation creep to diffusion creep. This process resulted in the rheological weakening of garnet websterites, which also affected the host peridotites.

2. Geological and Petrological Background

The Ulten zone (hereafter UZ) forms the northern part of the Tonale Nappe, belonging to the Austroalpine tectonic domain of the Eastern Alps (Figure 1a). It represents a high-grade basement unit containing slivers of amphibolitized eclogites (Del Moro et al., 1999; Tumiati et al., 2003) and peridotites that reached peak metamorphic conditions during the late Paleozoic Variscan orogeny (Godard et al., 1996; Herzberg et al., 1977; Hoinkes & Thöni, 1993; Martin et al., 1993; Obata & Morten, 1987; Tumiati et al., 2003, 2007).

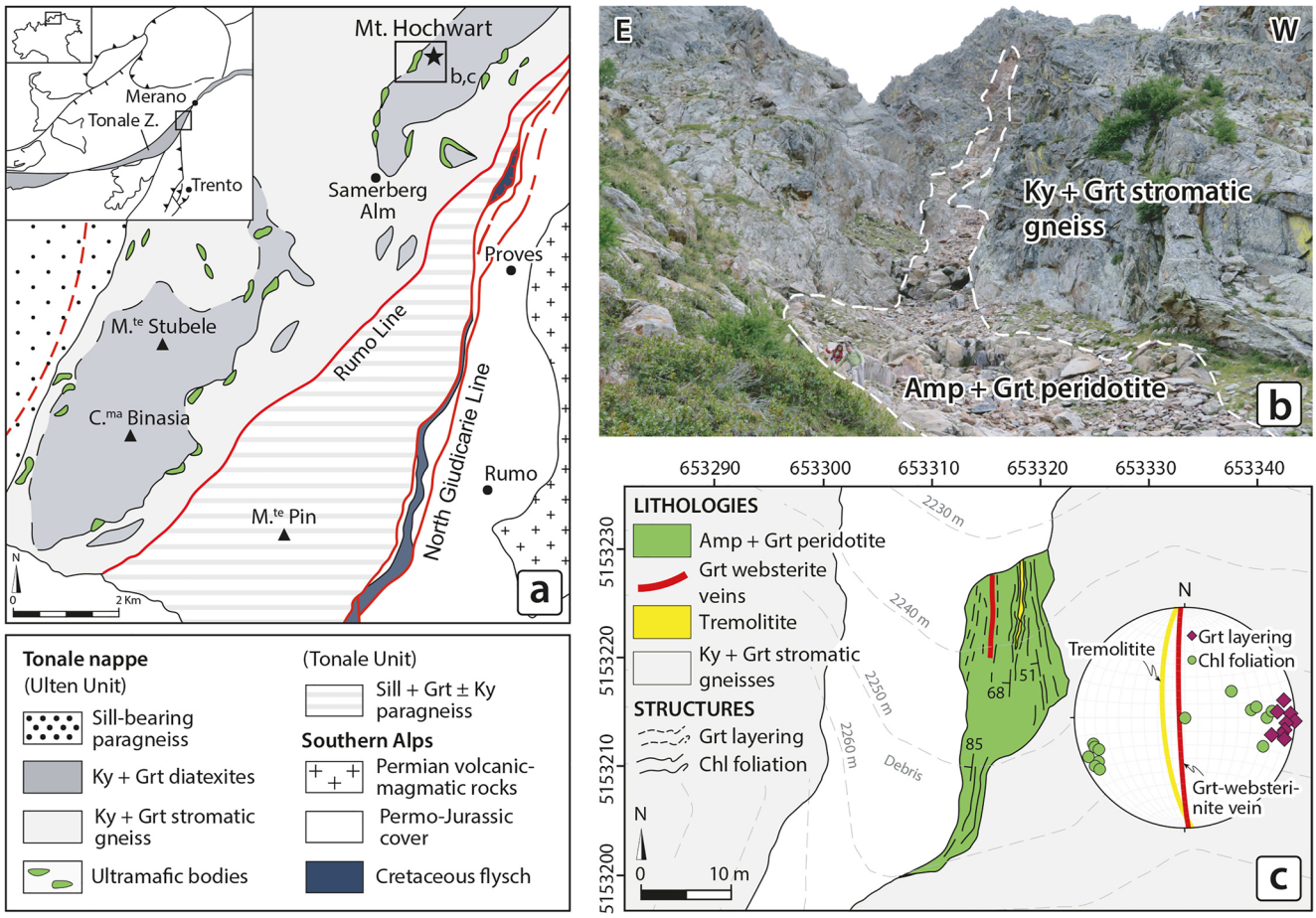

Figure 1. (a) Simplified geological map of Ulten Zone (UZ; Redrawn after Del Moro at al., 1999). The heavy rectangle is the framework for Figures 1b and 1c; (b) Mt. Hochwart amphibole + garnet peridotite body (N. Malaspina and S. Tumiati for scale); and (c) detailed geological map of the Mt. Hochwart amphibole + garnet peridotite body.

Mafic and ultramafic bodies are surrounded by mylonitic, garnet + kyanite stromatic gneisses, and garnet + kyanite diatexites (Ranalli et al., 2005). The felsic migmatites and the amphibolitized eclogites record a complex evolution from eclogite-, to granulite-, to amphibolite-facies conditions. Maximum pressures and temperatures experienced by migmatitic felsic rocks have been calculated at 1.5-2.5 GPa and 700-850 °C (Braga et al., 2007; Godard et al., 1996; Hauzenberger et al., 1996; Hoinkes & Thöni, 1993; Tumiati et al., 2003). Migmatization took place under fluid-absent conditions by phengite dehydration melting at a temperature of 850 °C and pressures of 1.5-2.5 GPa (Godard et al., 1996; Hauzenberger et al., 1996; Tumiati et al., 2003) and likely occurred either during prograde subduction or the early stages of exhumation after stromatic gneiss and diatexites reached the pressure peak (Tumiati et al., 2003).

In the field, peridotites occur as meters to hundreds of meters-long lenses aligned along a discontinuous band at the transition between the stromatic gneisses and the diatexites (Figure 1a and 1b). Peridotites show a transition from coarse protogranular spinel lherzolites (coarse-type of Obata & Morten, 1987) to finer-grained amphibole + garnet peridotites (fine- type of Obata & Morten, 1987). Thermobarometric estimates on spinel-facies assemblages yielded an equilibrium condition of P = 1.3–1.6 GPa and T = 1200 °C (Nimis & Morten, 2000). During this stage, peridotites were infiltrated by hydrous melts rising from the deep regions of the lithospheric mantle, precipitating coarse-grained websterites in the host peridotites (Nimis & Morten, 2000). These pyroxenites record a textural evolution similar to that of the host peridotites and change from coarse-grained websterites (clinopyroxene + orthopyroxene ± olivine) to finer-grained garnet websterites. The re-equilibration of websterites and peridotites in the garnet stability field is calculated to have occurred at P = 2.0–2.7 GPa and T = 850 °C (Braga & Sapienza, 2007; Malaspina & Tumiati, 2012; Nimis & Morten, 2000; Tumiati et al., 2003). At these conditions,

garnet formed at the expenses of spinel in peridotites, exsolved from porphyroclastic, high-T pyroxenes in both peridotites and websterites, and crystallized along the foliation of websterites and host peridotites. This evolution has been interpreted to reflect cooling and pressure increase of websterites and host peridotites due to the mantle corner flow from hot regions of the subcontinental lithospheric mantle to deeper and cooler mantle domains located at the top of the slab (Nimis & Morten, 2000).

The re-equilibration at high pressure of websterites and hosting peridotites was accompanied by intense shearing and fluid infiltration (Obata & Morten, 1987; Rampone & Morten, 2001). Indeed, hydration related to the high-pressure metamorphism promoted the formation of garnet-bearing assemblages in both websterites and peridotites (Obata & Morten, 1987), the crystallization of metasomatic minerals such as amphibole, phlogopite, dolomite, allanite, and dissakisite-(La) in peridotites (Lavina et al., 2006; Malaspina & Tumiati, 2012; Marocchi et al., 2009; Morten & Trommsdorff, 2003; Sapienza et al., 2009; Susini & Martin, 1996; Tumiati et al., 2005), and amphibole in websterites, suggesting recrystallization under the influence of slab-derived fluids (Rampone & Morten, 2001; Scambelluri et al., 2006; Tumiati et al., 2007).

Finally, the exhumation and re-equilibration at low pressure of the UZ peridotites are documented by spinel + orthopyroxene + clinopyroxene + amphibole and orthopyroxene + amphibole + clinopyroxene kelyphites around garnet and the complete replacement of garnet by chlorite pseudomorphs or by coarse-grained amphibole + spinel aggregates (Martin et al., 1998; Godard & Martin, 2000).

3. Materials and Methods

Electron backscattered diffraction (EBSD) analyses on clinopyroxene and orthopyroxene in garnet websterites were carried out on a JEOL 6610 VP-SEM equipped with an Oxford Instruments Nordlys Nano EBSD detector and a JEOL 7001 FEG SEM equipped with a NordLys Max EBSD detector (AZTec acquisition software, Oxford Instruments) at the Electron Microscope Centre of the University of Plymouth, and a Zeiss Gemini 500 FEG SEM equipped with an e-Flash EBSD detector (Quantax EBSD acquisition software, Bruker) at the University of Milano Bicocca. EBSD patterns were acquired on rectangular grids with step sizes of 0.14, 1.3, 2.0, and 2.8 μm. Working conditions were 20 kV accelerating voltage, 10 nA of beam current, high vacuum, 70° sample tilt, and working distance between 17 and 23 mm. A detailed description of the EBSD sample preparation and post-processing methods is reported in the supporting information (Text S1 in Supporting Information S1). For grain-size measurements, grain boundaries were manually traced on backscattered electron (BSE) and secondary electron (SE) images or derived from crystallographic orientation data acquired by EBSD analyses. In this latter case, grain boundaries were defined for critical misorientations of 10°, while they were considered for subgrain-size analysis, only closed subgrain boundaries were defined for critical misorientation angles of 2°. The grain size and the subgrain size were measured using the mean linear intercept method following the American Society for Testing and Materials ASTM E112-12 procedure. Test lines were traced parallel, normal, and randomly oriented with respect to the foliation. A stereological correction factor of 1.5 was applied (Linckens et al., 2014). Results are listed in Table S1.

Transmission electron microscopy (TEM) investigations were performed at the Friedrich Schiller University Jena. For TEM characterization, we prepared thin sections with an acetone-soluble glue. Copper grids were mounted with two-component resin on the free surface of thin sections at sites of interest. These grids including the interesting areas were removed from slides by acetone dissolution. The sample grids were then Ar ion-thinned in a Gatan Duomill ion milling machine at 4.5kV and 1mA until electron transparency was reached. TEM characterization of defect microstructures was carried out with a 200 kV FEI Tecnai G2 F20 TEM, using conventional bright-field and dark-field imaging techniques in combination with selected area electron diffraction (SAED). To search larger areas for lattice defects, we have also used the high-angle annular dark-field (HAADF) detector at low magnification scanning transmission electron microscopy (LM-STEM) mode with a very long camera length to obtain diffraction contrast images. The mineral identification was aided by energy-dispersive X-ray (EDX) spectra using an Oxford X-MaxN 80T SDD system.

Thermodynamic modeling was performed with the software package Perple_X (Connolly, 2005), using the thermodynamic database of Holland and Powell (1998) revised in 2002 (hp02ver.dat) and the following solution models described by Holland and Powell (1998) (HP), Holland and Powell (2003) (I1, HP, and C1), and Dale et al. (2000) (D): Gt(HP) for garnet, Opx(HP) for orthopyroxene, O(HP) for olivine, Omph(HP) for Ca-Na

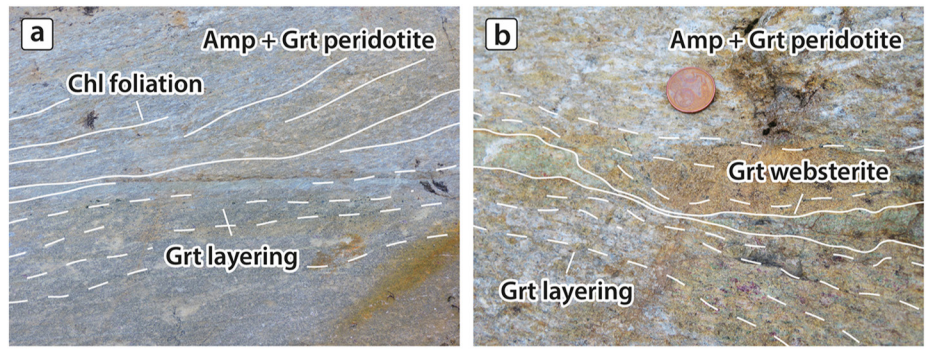

Figure 2. Structures of amphibole + garnet peridotites and garnet websterites of UZ. (a) Garnet layering transposed by a chlorite foliation in amphibole + garnet peridotites; (b) garnet websterite vein transposed along the garnet layering of amphibole + garnet peridotites.

clinopyroxene, Sp(HP) for spinel, Ca-Amp(D) for calcic amphibole, Chl(HP) for chlorite, and Pl(I1, HP) for ternary feldspars. The water equation of state was taken from Holland and Powell (1998).

4. Results

4.1. Field Observations

In the northern sectors of the UZ, amphibole + garnet peridotite lenses and country stromatic gneisses are well exposed along a steep gully on the western ridge of the Mt. Hochwart (Figure 1a and 1b). The peridotite body is continuous from the base of the gully (2233 m) up to the Hochwart Pass (2475 m). Amphibole + garnet peridotites (green in Figure 1c) have a porphyroclastic texture with coarse (up to 1-2 cm) amphibole and garnet porphyroclasts (reaching up to 9 cm in diameter in the inner part of the peridotite body) embedded in a finer grained matrix consisting of olivine, orthopyroxene, amphibole, and rare clinopyroxene. Garnets are invariably mantled by spinel + orthopyroxene + clinopyroxene ± amphibole kelyphitic coronas or replaced by chlorite pseudomorphs. Peridotites display a steep W-dipping compositional layering consisting of garnet-rich and garnet-poor bands locally transposed by a chlorite foliation that becomes more penetrative at the contact with the surrounding stromatic gneisses (Figure 2a). Peridotites include centimeter-thick garnet websterite veins (red in Figure 1c; Figure 2b), which occur parallel to the garnet foliation in the peridotite. They are characterized by clinopyroxene and orthopyroxene porphyroclasts (up to 5 mm) enclosed in a finer grained matrix composed of emerald-green Cr-diopside, orthopyroxene, amphibole, and garnet. The anisotropic fabric of the garnet websterites is marked by garnet-rich and garnet-poor levels that dip to the west parallel to the garnet layering in the host peridotite. Peridotites also contain meter scale tremolitite layers (yellow in Figure 1c) consisting of tremolite (80-90 vol%) with subordinate chlorite pseudomorphs after garnet and minor Mg hornblende. Tremolitites are strongly stretched and boudinaged parallel to chlorite foliation in the peridotite.

The contact between peridotites and country stromatic gneisses is often marked by metasomatic reaction zones with a composite structure consisting of an inner tremolite-rich cm-thick layer on the peridotite side and an outer phlogopite-rich front toward the host gneiss (see also Marocchi et al., 2009, 2010; Tumiati & Martin, 2003; Tumiati et al., 2007).

The country gneisses (light gray in Figure 1c) have a stromatic texture characterized by cm-spaced bands of quartz + plagioclase + K-feldspar ± garnet ± kyanite leucosomes and garnet + kyanite + biotite melanosomes (restites) transposed along the regional foliation (for a detailed description of these rocks, see also Del Moro et al., 1999; Martin et al., 1998; Tumiati et al., 2003).

4.2. Microstructures

Representative samples of garnet websterites have been selected for this study. Sample location and coordinates are given in Figure S1 of supporting information. Mineral abbreviations are from Whitney and Evans (2010).

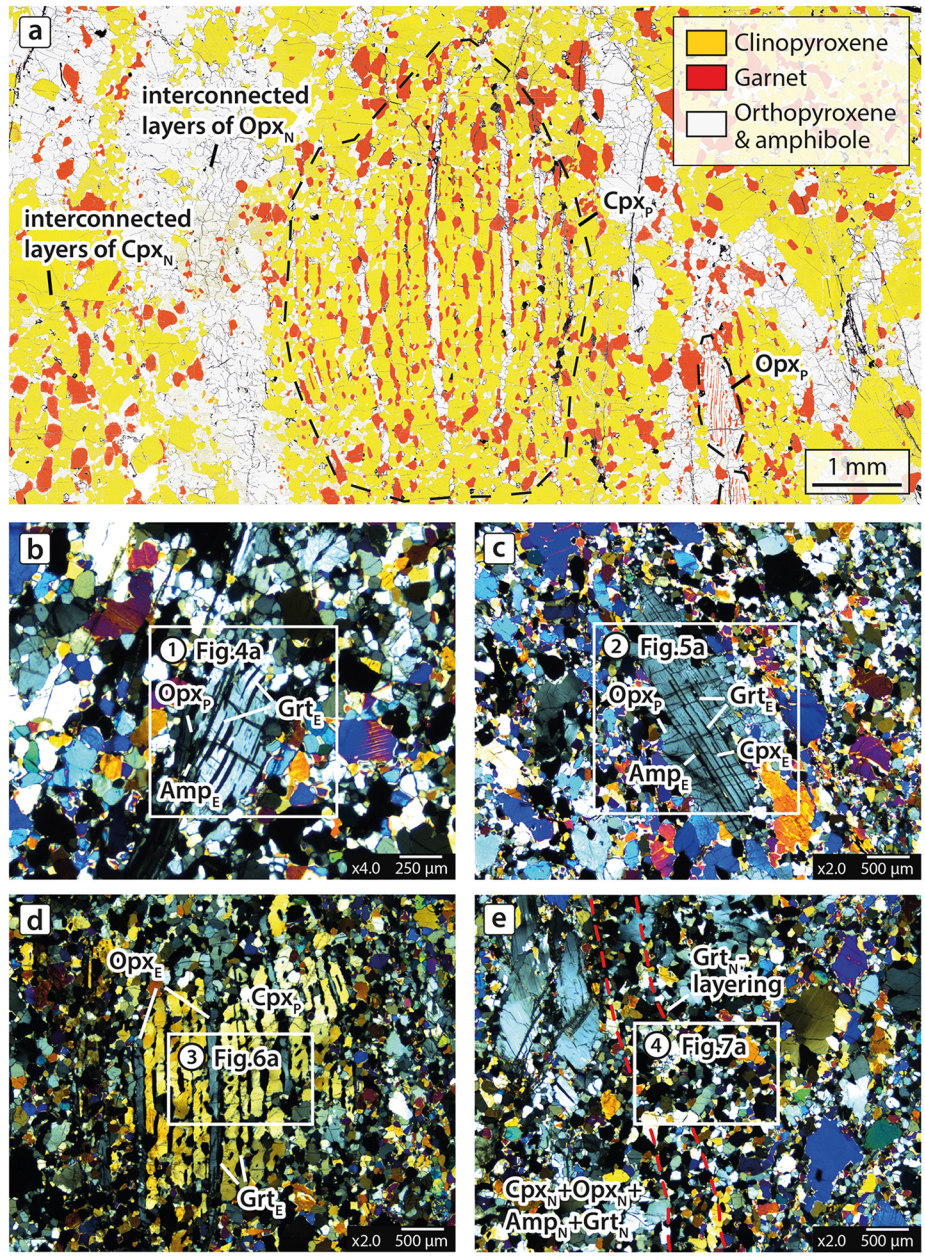

Figure 3. (a) Phase map showing the websterite texture with clinopyroxene (yellow) and garnet (red) distribution. Orthopyroxene and interstitial amphibole are represented in light gray tones. The map was obtained from segmentation and filtering of high-contrast BSE (Backscattered Electrons) images stitched together to obtain a field of view of c. 12 x 7 mm. XPL photomicrographs of garnet websterites of Mt. Hochwart: (b) coarse Opx_P with Grt_E and Amp_E exsolutions along curved crystal planes (sample UT23); (c) porphyroclastic Opx_P with exsolutions of Grt_E, Amp_E, and Cpx_E (sample UT23); (d) porphyroclastic Cpx_P with exsolution lamellae of Grt_E and Opx_E (sample UT23); and (e) Grt_N layering in garnet websterite UT23. The Grt_N layering is oriented parallel to the direction of the Grt_E exsolutions in Cpx_P. The white rectangles indicate the site of the EBSD maps shown in Figures 4–7. The circled numbers denote the microstructural domains.

4.2.1. Garnet Websterites

Garnet websterites have a porphyroclastic texture with coarse (up to 3 mm) orthopyroxene (Opx_P) and clinopyroxene (Cpx_P) porphyroclasts surrounded by finer grained, dynamically recrystallized, neoblastic clinopyroxene (Cpx_N) and orthopyroxene (Opx_N) organized in interconnected layers (Figure 3a), and minor amounts of amphibole (Amp_N) and garnet (Grt_N). To fully describe the porphyroclastic and neoblastic assemblages and

the different internal deformation microstructures, four different microstructural domains have been identified (Figures 3b–3d).

The Opx_P (domains 1 and 2; Figures 3b and 3c) varies in length from 1.5 to 3 mm and contains exsolution lamellae of garnet (Grt_E) clinopyroxene (Cpx_E) and amphibole (Amp_E). It shows intracrystalline deformation in the form of undulose extinction, kink bands, and core-and-mantle microstructures where the core of the porphyroclast grades outward into subgrains and newly recrystallized grains. The elongation of Opx_P is parallel to the trace of the compositional layering of the rock.

The coarse Cpx_P (domain 3; Figure 3d) displays undulose extinction and contains exsolution lamellae of Grt_E, orthopyroxene (Opx_E), and Amp_E. The Opx_E lamellae are 50-100 μm thick and up to 3-mm long, while Grt_E exsolutions are typically small with aspect ratios varying from 1:1 to 5:1. The exsolved Amp_E occurs as an interstitial phase at Cpx_P-Opx_E-Grt_E grain boundaries or triple junctions (Figure S2).

Both recrystallized Cpx_N and Opx_N (domain 4; Figure 3e) are optically strain-free and contain no exsolution lamellae. Garnet occurs as small crystals (up to 600 μm) in textural equilibrium with the neoblastic $Cpx_N + Opx_N + Amp_N$ assemblage and defines the compositional layering of the rock. Notably, the garnet layering is parallel to the orientation of the garnet exsolution lamellae within orthopyroxene and clinopyroxene (Figure 3e).

4.3. EBSD Analysis

The results of EBSD analysis of the different microstructural domains of garnet websterites are displayed in Figures 4–7 (see Figure 3 for the location of the EBSD maps):

(i) Domain 1 includes a deformed orthopyroxene porphyroclast surrounded by finer grained recrystallized orthopyroxene neoblasts (Figure 3b);
(ii) Domain 2 shows a porphyroclastic orthopyroxene with a core-and-mantle microstructure (Figure 3c);
(iii) Domain 3 comprises a clinopyroxene porphyroclast (Figure 3d);
(iv) Domain 4 is representative of the recrystallized clinopyroxene grains around the porphyroclastic clinopyroxene of domain 3 (Figure 3e).

4.3.1. Domain 1

The coarse-grained Opx_P is oriented with the [010] axes subparallel to the stretching lineation and the (100) planes subparallel to the foliation (Figure 4b). The distortion of the crystal lattice is characterized by gradual increments of misorientations <2° and with sharper misorientation jumps corresponding to low-angle boundaries (2°−10°), with a total distortion across the porphyroclast of 16° over a distance of 600 μm (profile AA' in Figure 4d). However, low-angle boundaries are scarce and are mostly restricted close to the garnet exsolutions (Figure 4a). The misorientation axes for low-angle misorientations show two maxima close to the center of the pole figure and close to the pole to the foliation (Figure 4c). These misorientation axes preferentially cluster close to the [001] and the [100] axes in crystal coordinates (Figure 4c). The high-angle (>10°) misorientation axes distributions not only resemble the patterns of the low-angle misorientation axes in sample and crystal coordinates (Figure 4c), but also show other minor clusters in different orientations, which are particularly evident in crystal coordinates.

The transition from porphyroclastic Opx_P to the finer grained, neoblastic Opx_N is marked by large misorientation angles between the new grains and the neighboring porphyroclast (profile BB' in Figure 4e). The recrystallized grains display common quadruple junctions (white arrow in Figure 4a), have internal misorientations lower than 3° (Figure S3), and are strongly misoriented with respect to each other (profile BB' in Figure 4e). The Opx_N has a weak CPO controlled by the parent porphyroclast (Figure 4b), showing a concentration of the [010] axes relatively close to the stretching lineation and a cluster of the (100) planes subparallel to the foliation (Figure 4b). The misorientation angle distribution of correlated pairs displays higher frequency than the random-pair distribution for misorientations <60° and lower frequency for misorientations >60°. This pattern is also evident in the uncorrelated-pair distribution, but with smaller deviations from the random theoretical curve (Figure 4f).

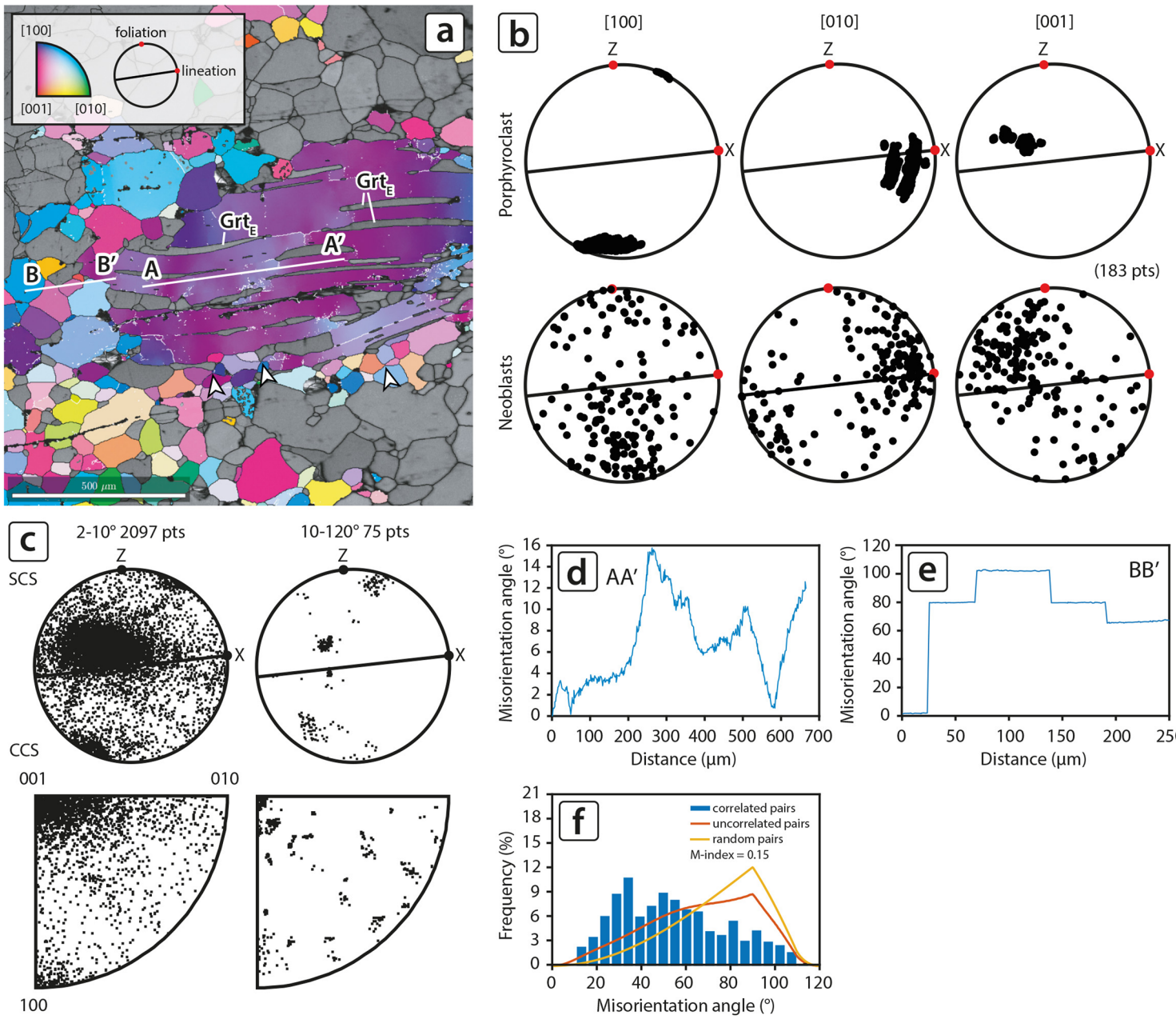

Figure 4. EBSD map and CPO data of Opx_P and Opx_N in garnet websterite UT23. (a) EBSD-derived inverse pole figure map with respect to Z sample direction. Grain boundaries are colored in black. Subgrain boundaries are colored in white. White arrows indicate the presence of quadruple junctions in the recrystallized matrix; (b) pole figures of porphyroclastic (all data points) and neoblastic orthopyroxene. Upper hemisphere, equal area projection. Contoured plots are reported in Figure S4; (c) misorientation axis distributions for porphyroclastic orthopyroxene in sample (SCS, upper row) and crystal (CCS, lower row) coordinate system; (d) cumulative misorientations relative to the first point (profile AA'); (e) cumulative misorientations relative to the first point (profile BB'); and (f) misorientation angle distribution for neoblastic orthopyroxene.

4.3.2. Domain 2

The porphyroclastic Opx_P is oriented with the [010] axes subparallel to the stretching lineation and the (100) planes subparallel to the foliation (Figure 5b), consistently with the Opx_P grain shown in Figure 4. The analyzed porphyroclast displays a strong internal distortion with cumulative misorientations across the entire crystal as large as 32° (profile AA' in Figure 5d). However, low-angle boundaries are scarce and are mainly confined close to the margin of the porphyroclast. In sample coordinates, the misorientation axes distribution for low-angle misorientations displays a clear maximum close to the center of the pole figure, while in crystal coordinates, it

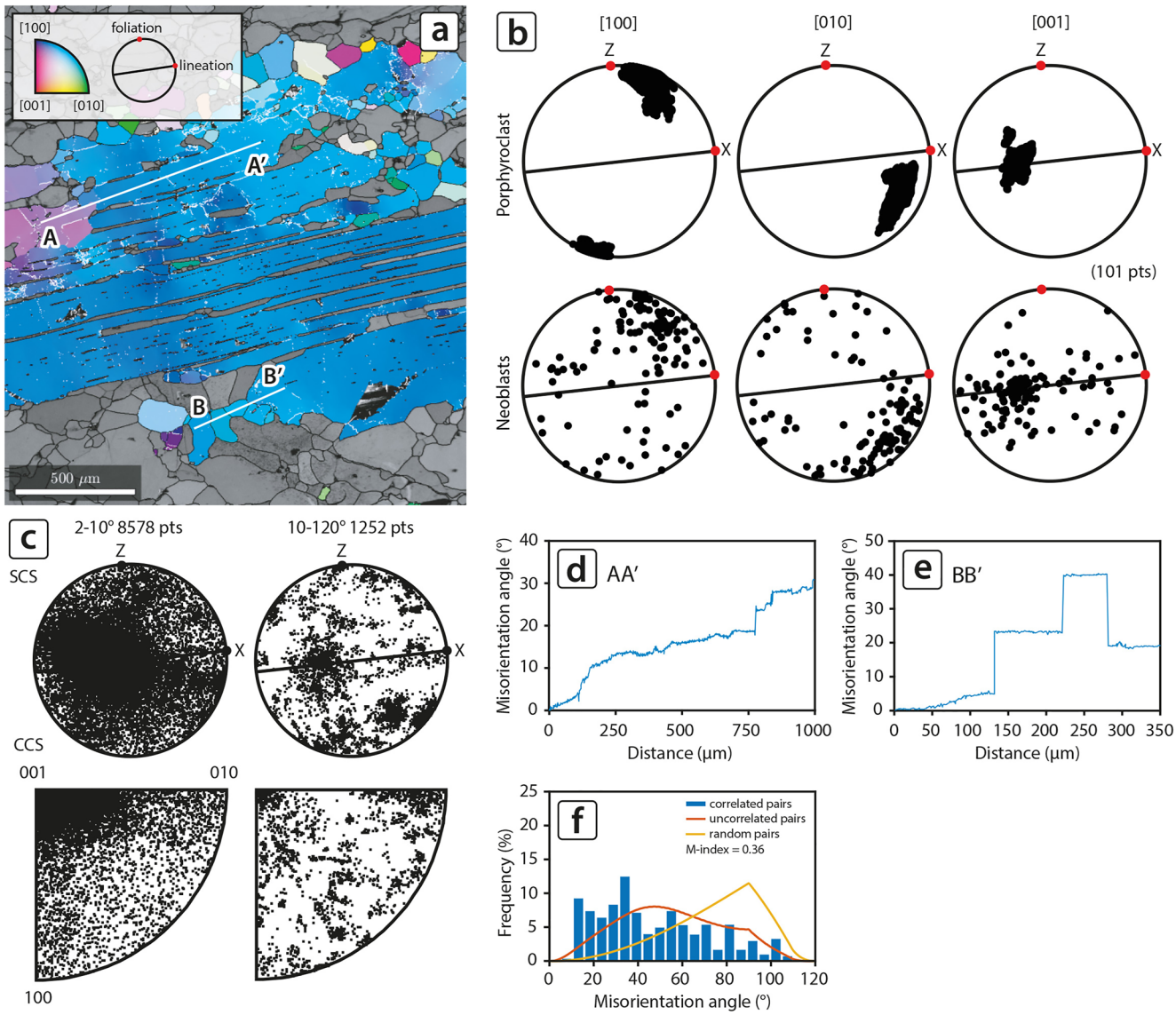

Figure 5. EBSD map and CPO data of Opx_P and Opx_N in garnet websterite UT23. (a) EBSD-derived inverse pole figure map with respect to Z sample direction. Grain boundaries are colored in black. Subgrain boundaries are colored in white; (b) pole figures of porphyroclastic (all data points) and neoblastic orthopyroxene. Upper hemisphere, equal area projection. Contoured plots are reported in Figure S6; (c) misorientation axis distributions in sample (upper row) and crystal (lower row) coordinate systems (abbreviations same as in Figure 4c); (d) cumulative misorientations relative to the first point (profile AA'); (e) cumulative misorientations relative to the first point (profile BB'); and (f) misorientation angle distribution for neoblastic orthopyroxene.

forms a cluster close to [001] axis (Figure 5c). The high-angle misorientation axes in sample coordinates display a principal maximum close to (but slightly offset from) the center of the pole figure, and few minor scattered maxima, including a weak maximum close to the pole to the foliation (Figure 5c). In crystal coordinates, these misorientation axes preferentially cluster close to the [001] and [010] axes (Figure 5c).

The transition from porphyroclastic to finer grained, recrystallized Opx_N is marked by large misorientation angles, usually >20° (profile BB' in Figure 5e). The neoblastic Opx_N is almost strain-free (Figure S5) and has a CPO strongly controlled by the adjacent porphyroclast since they show the [010] axes aligned subparallel to the lineation and the (100) planes oriented subparallel to the foliation (Figure 5b). The misorientation angle distributions of both correlated and uncorrelated pairs show higher frequency than the random-pair distribution for misorientations <60° and lower frequency for misorientations >60° (Figure 5f).

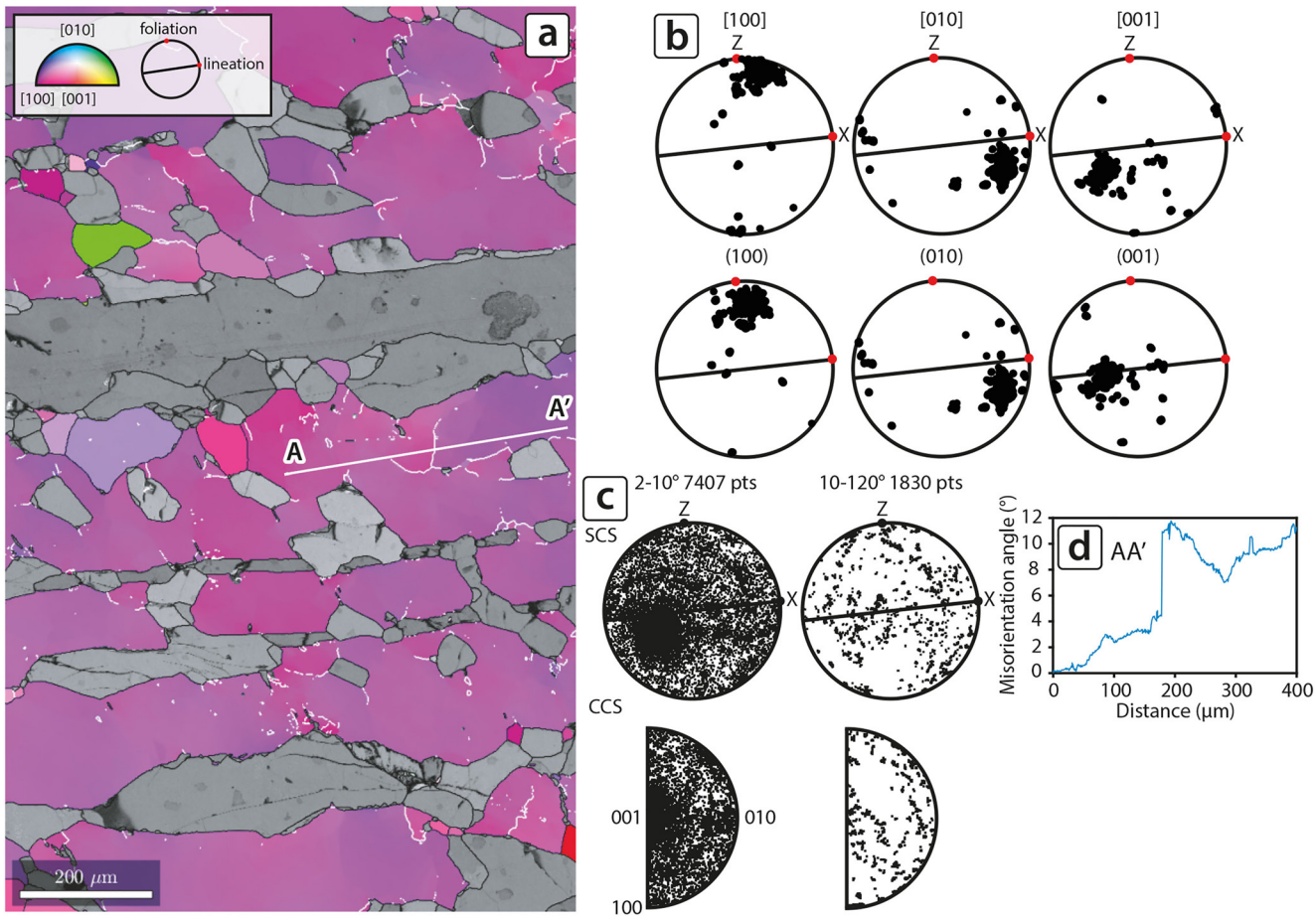

Figure 6. EBSD map and CPO data of Cpx_P in garnet websterite UT23. (a) EBSD-derived inverse pole figure map with respect to Z sample direction. Grain boundaries are colored in black. Subgrain boundaries are colored in white; (b) pole figures (all data points). Upper hemisphere, equal area projection; (c) misorientation axis distributions in sample (upper row) and crystal (lower row) coordinate systems (abbreviations same as in Figure 4c); and (d) cumulative misorientations relative to the first point (profile AA').

4.3.3. Domain 3

Porphyroclastic Cpx_P is oriented with the [010] axes subparallel to the stretching lineation and the (100) planes subparallel to the foliation (Figure 6b). It displays an internal distortion with cumulative misorientations as large as 12° (profile AA' in Figure 6d). The density of low-angle boundaries is very low, consistently with a limited development of subgrains. The low-angle misorientation axes in sample coordinates display a maximum close (but slightly offset from) to the center of the pole figures (Figure 6c). These misorientation axes cluster close to the [001] axis in crystal coordinates (Figure 6c). The high-angle misorientation axes distributions in both sample and crystal coordinates do not show any clear clustering (Figure 6c).

4.3.4. Domain 4

The fine-grained Cpx_N displays a weak CPO slightly controlled by the CPO of the adjacent porphyroclast, showing a weak maximum of the [010] axes close to the stretching lineation and a concentration of the (100) planes subparallel to the foliation (Figure 7b). The fine-grained aggregate of Cpx_N + Opx_N + Amp_N + Grt_N displays common quadruple junctions (Figures 7c and 7d) and aligned, straight grain boundaries (Figure 7e). The recrystallized clinopyroxene grains usually have internal misorientation lower than 3° (Figures 7c–f and S7) and are strongly misoriented with respect to each other (profile AA' in Figure 7f). The misorientation angle distributions of correlated and uncorrelated pairs deviate from the random theoretical curve, showing an excess in misorientation angles lower than 90° and a deficit in misorientation angles greater than 90° (Figure 7g).

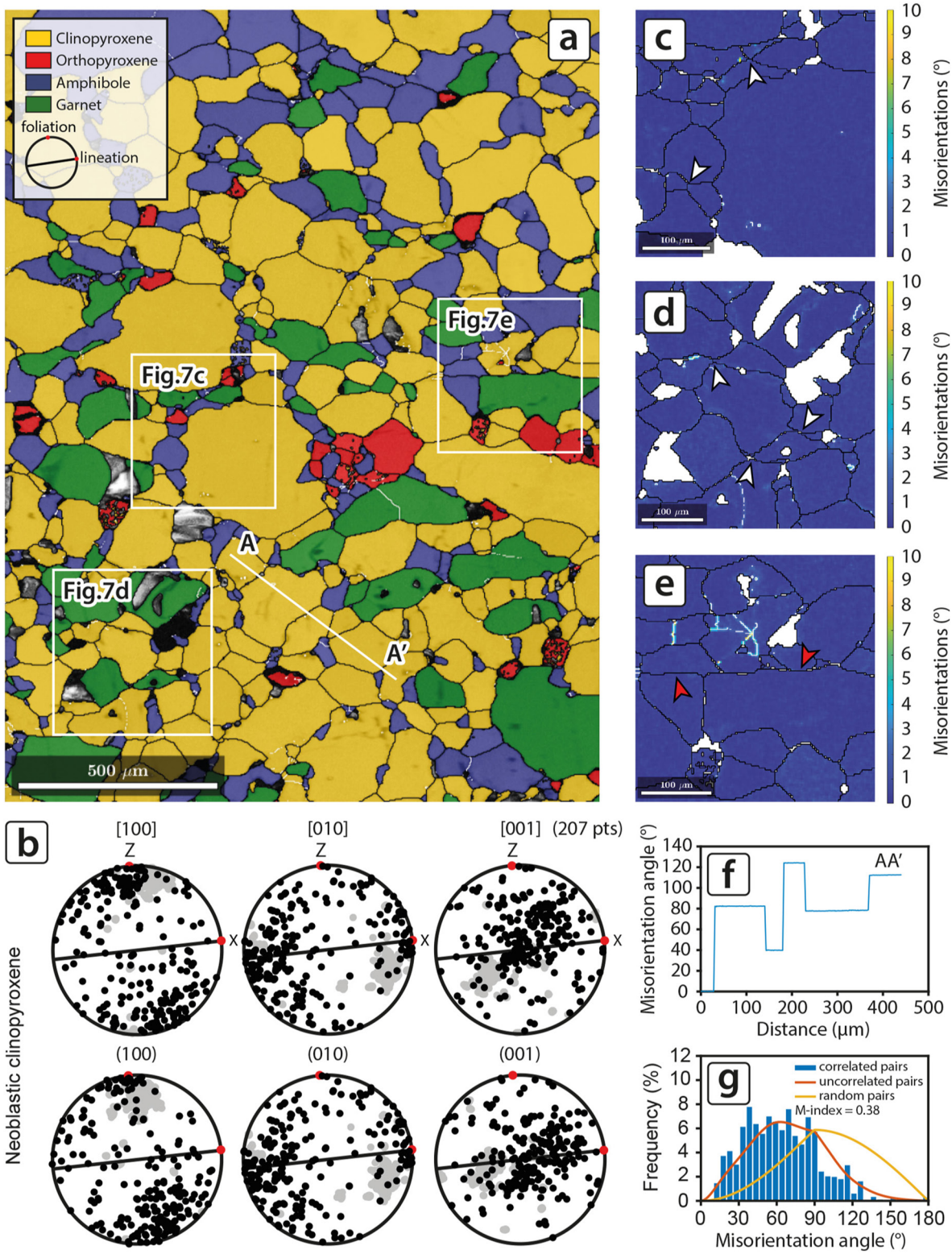
a
Clinopyroxene
Orthopyroxene
Amphibole
Garnet
foliation
lineation
Fig.7c
Fig.7d
Fig.7e
A
A′
500 μm
b
[100]
[010]
[001] (207 pts)
Z
X
Neoblastic clinopyroxene
(100)
(010)
(001)
c
d
e
100 μm
Misorientations (°)
0 1 2 3 4 5 6 7 8 9 10
f
AA′
Misorientation angle (°)
0 20 40 60 80 100 120 140
0 100 200 300 400 500
Distance (μm)
g
correlated pairs
uncorrelated pairs
random pairs
M-index = 0.38
Frequency (%)
0 2 4 6 8 10 12
0 30 60 90 120 150 180
Misorientation angle (°)

Figure 7.

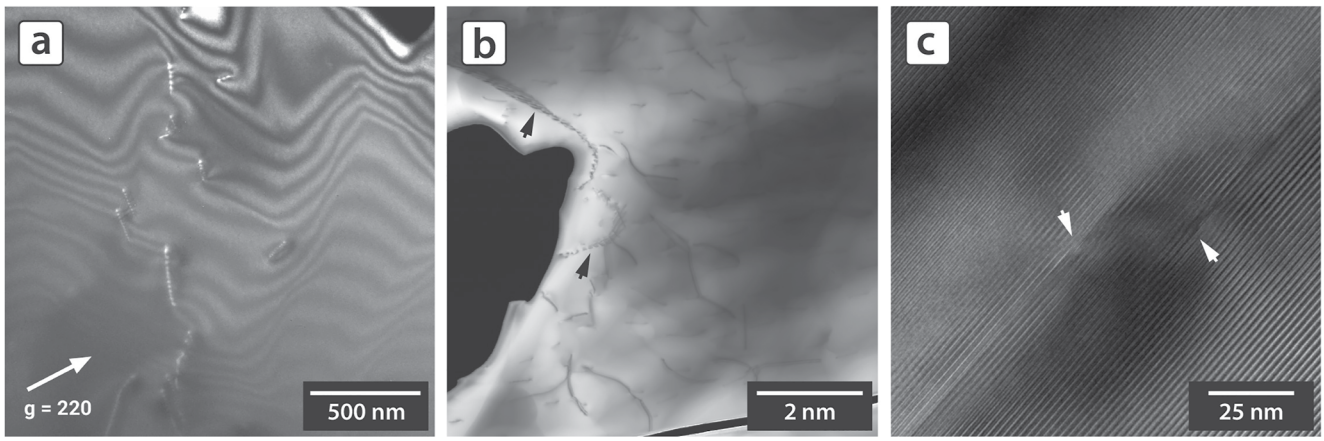

Figure 8. (a) Dark-field weak beam, (b) LM-STEM dark field, and (c) high-resolution TEM images of dislocations in porphyroclastic orthopyroxene from domain 2. Image (a) was taken with the 220 reflection, showing sharp well-visible dislocations. The STEM image in (b) shows a larger and thicker area of orthopyroxene with subgrain boundaries (black arrows) and partly entangled dislocations indicating interactions between them. The HRTEM image in (c) was taken along the [0-13] zone axis and shows the 1.8-nm lattice fringes. Two dislocation lines are visible to lie in projection in the (100) plane.

4.4. TEM Characterization

Bright-field and dark-field TEM as well as STEM imaging were employed to observe lattice defects in porphyroclastic orthopyroxene and to verify the slip systems that were activated during its deformation. Despite the distinct deformation of the host rock, orthopyroxene contains free dislocations only in moderate densities of $2\text{-}5{\cdot}10^{12}$ m^{-2} (Figure 8). However, STEM images show that there are several subgrain boundaries, which indicate that numerous dislocations climbed and recovered to form these internal boundaries (Figure 8b). The entire orthopyroxene is thus subdivided into a mosaic of several µm-sized sub-grains forming mutual low-angle boundaries between each other.

A closer look at the dislocation microstructures shows overall that dislocation lines are often similarly aligned, but at nodes, dislocations also meet with different line directions, suggesting that not only one slip system was activated. To further evaluate the Burgers vector of most dislocations, we have performed weak-beam TEM imaging using the g–$b = 0$ criterion (Figure 8a). TEM images were systematically taken with reflections occurring in the [−112] zone axis diffraction pattern. When employing $g = 220$ (see Figure 8a), dislocations are well visible, excluding $b = [001]$ as Burgers vector. Dislocation are also well visible with $g = 0\text{-}21$, while they became invisible when using $g = 402$. In conclusion, this means that the Burgers vector of most dislocations is $b = [010]$, in line with EBSD measurements. The unequivocal determination of the slip plane turned out to be complicated because mostly straight dislocation lines were strongly inclined to the beam direction, making indexing of their directions difficult. Therefore, we used high-resolution imaging (HRTEM) to visualize in which plane the dislocation lines project. The lattice fringe image in Figure 8c shows two projected dislocation lines that lie within the (100) plane, indicating this is the slip plane. Altogether, the TEM observations thus corroborate that the major slip system is (100)[010].

5. Discussion

5.1. Deformation Mechanisms

The Opx_P is interpreted to deform by dislocation glide and creep on the (100)[010] slip system, as indicated by microstructures, i.e., undulose extinction and crystal bending, the dominant [001] misorientation axis, and by our

Figure 7. EBSD map and CPO data of the fine-grained matrix of garnet websterite UT23. The white rectangles indicate the sites of Figures 7c, 7d, and 7e. (a) Phase map. Grain boundaries are colored in black. Subgrain boundaries are colored in white; (b) pole figures of neoblastic clinopyroxene in upper hemisphere, equal area projection. In light gray is reported the orientation of the adjacent Cpx_P of domain 3 (Figure 6). Contoured plots are reported in Figure S8; (c, d, e) kernel-average misorientation (KAM) maps showing the local misorientation of each pixel based on a 5x5 grid of neighbouring pixels. Quadruple junctions and aligned, straight grain boundaries are indicated by white and red arrows, respectively; (f) cumulative misorientations of neoblastic clinopyroxene relative to the first point (profile AA'); and (g) misorientation angle distributions of neoblastic clinopyroxene.

TEM observations (Figure 8). Compared to the (100)[001], which is considered the main activated slip system in orthopyroxene (Soustelle et al., 2010; Tommasi et al., 2008; Skemer et al., 2006; Xu et al., 2006; Ishii & Sawaguchi, 2002; Vauchez and Garrido, 2001; Mainprice et al., 2000; Christensen and Lundquist, 1982), the (100)[010] has not been frequently reported in literature. However, rare natural occurrences (Jung et al., 2010; Kohlstedt & Vander Sande, 1973; Nazè et al., 1987; Skrotzki, 1990, 1994), deformation experiments (Nazè et al., 1987; Raleigh et al., 1971), room temperature indentations of enstatite (Van Duysen et al., 1985), and numerical simulations (Jahn & Martonak, 2008) suggest that orthopyroxene can deform and rotate around the [001] until the (100) tends to be parallel to the XY foliation plane and the Burgers vector **b** [010] becomes parallel to the stretching lineation, as observed in our orthopyroxene porphyroclasts.

The core-and-mantle microstructure of Opx_P of domain 2 suggests that dislocation creep on the (100)[010] was accommodated by subgrain rotation (SGR) recrystallization. In particular, we observe that low-angle boundaries are mostly restricted close to the rim of the porphyroclast, reflecting a progressive accumulation of misorientations from the core of the Opx_P to the mantle of the newly recrystallized grains.

The recrystallized Opx_N is interpreted to deform primarily by grain boundary sliding (GBS), as indicated by the common occurrence of quadruple junctions in the recrystallized Opx_N matrix (Figure 4a). The Opx_N locally forms a mosaic-like texture with 120° triple junctions, suggesting that annealing and grain growth occur during/after deformation by GBS. This is also supported by the average grain size of the recrystallized Opx_N (73.7 μm), which is slightly larger than the average size of the internal subgrains of porphyroclastic Opx_P (57.5 μm; Table S1).

The Cpx_P is interpreted to deform by dislocation glide and creep, as evidenced by the undulose extinction and the development of subgrains, whereas the recrystallized Cpx_N shows evidence for GBS, including the occurrence of quadruple junctions (Figures 7c and 7d) and aligned, straight grain boundaries in the recrystallized Cpx_N matrix (Figure 7e). In particular, the quadruple junctions represent evidence for grain neighbor switching during GBS (Ashby & Verrall, 1973; Maruyama & Hiraga, 2017), while straight grain boundaries represent the sliding surfaces that were active during the relative movement of neighbor grains (Boullier & Gueguen, 1975; Miranda et al., 2016; White, 1977, 1979). In addition, the movement of grains during neighbor switching requires a rotational component of motion, which produces an increase in misorientations between adjacent grains (e.g., Bestmann & Prior, 2003; Svahnberg & Piazolo, 2010). This is consistent with our observation of large misorientation angles between neighbor recrystallized Cpx_N (Figure 7f). In summary, our microstructural observations, together with the low internal strain and the dispersion of CPO and misorientation axes for large misorientations, suggest that the main deformation mechanism of Opx_N and Cpx_N was diffusion-accommodated GBS (i.e., diffusion creep).

5.2. Piezometry and Rheological Model

In this section, we report the effects of the transformation of the coarse-grained Opx_P and Cpx_P into the finer grained Opx_N and Cpx_N on the bulk rheology of the UZ garnet websterites. Based on the deformation mechanisms identified from microstructures, that is, dislocation glide and creep in the porphyroclasts and diffusion creep in the finer grained neoblasts, deformation mechanism maps have been calculated for ortho- and clinopyroxene and plotted as grain size versus differential stress and differential stress versus strain rate diagrams (Figure 9).

The flow law of Bystricky et al. (2016) has been used to calculate the dislocation creep component of the total strain rate for orthopyroxene:

$$\dot{\varepsilon} = A_{dis}\ \sigma^{n_{dis}}\ e^{-\frac{Q_{dis}}{RT}} \quad (1)$$

where $\dot{\varepsilon}$ is the strain rate (s^{-1}), σ is the differential stress (MPa), n is the stress exponent, T is the temperature (K), R is the gas constant ($JK^{-1}mol^{-1}$), and A_{dis}, ($MPa^{-3}s^{-1}$) n_{dis}, and Q_{dis} ($Jmol^{-1}$) are empirical parameters for the pre-exponential term, the stress exponent, and the activation energy for dislocation creep, respectively.

The contribution of diffusion creep in orthopyroxene has been calculated using the flow law proposed by Bruijn and Skemer (2014):

$$\dot{\varepsilon} = C_m(T)\ \sigma\ d^{-p} \quad (2)$$

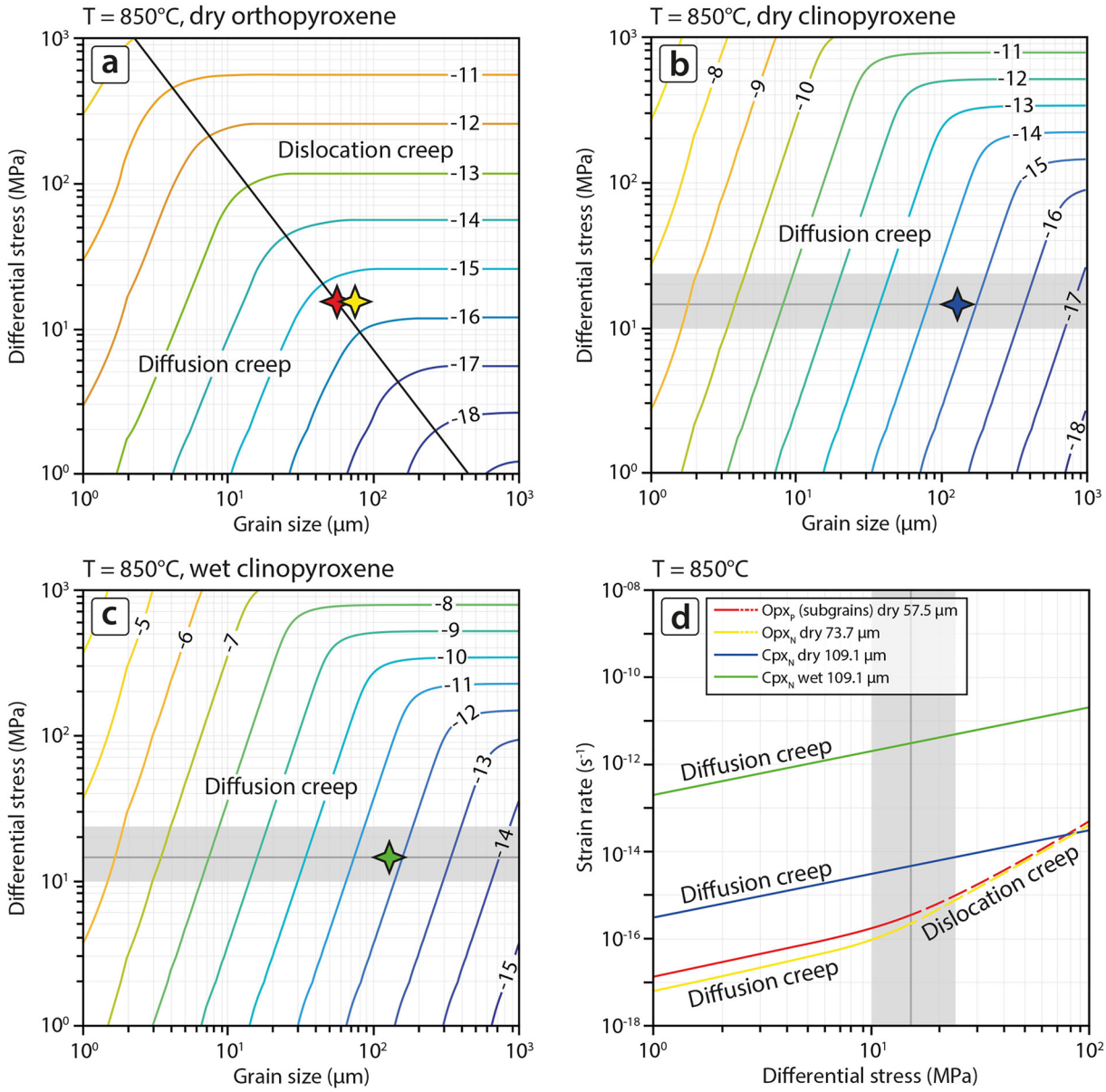

Figure 9. (a) Grain size versus differential stress map with contoured strain rate curves for dry orthopyroxene. The black solid line is the piezometer by Linckens et al. (2014). The red star corresponds to the size of subgrains in Opx_P (57.5 μm), while the yellow star represents the recrystallized Opx_N (73.7 μm); (b, c) Grain size versus differential stress map with contoured strain rate curves for dry (blue star) and wet (green star) clinopyroxene (109.1 μm); (d) strain rate versus differential stress diagram calculated for orthopyroxene (only dry) and clinopyroxene (wet and dry). The red line is the curve calculated for the subgrain size in Opx_P (57.5 μm). The yellow curve represents the recrystallized Opx_N (73.7 μm). Solid and dashed curves describe the deformational behavior of orthopyroxene in the diffusion creep and dislocation creep regimes, respectively. The blue and green solid curves have been calculated for recrystallized Cpx_N (109.1 μm) at dry and wet conditions, respectively. The gray transparent field (width includes errors) represents the differential stress derived from the orthopyroxene piezometer by Linckens et al. (2014). Deformation mechanism maps have been calculated at 850 °C. Other details on the derivation of the deformation mechanism maps are given in Section 4.2 of the main text and in Table S2.

where $\dot{\varepsilon}$ is the strain rate (s^{-1}), σ is the differential stress (MPa), $C_m(T)$ is the temperature-dependent variable ($s^{-1}MPa^{-1}\mu m^3$), d is the grain size (μm), and p is the grain-size exponent.

Differential stress during deformation was estimated using the grain-size piezometer for orthopyroxene of Linckens et al. (2014):

$$\sigma_{diff} = 2939\ d^{-1.308} \quad (3)$$

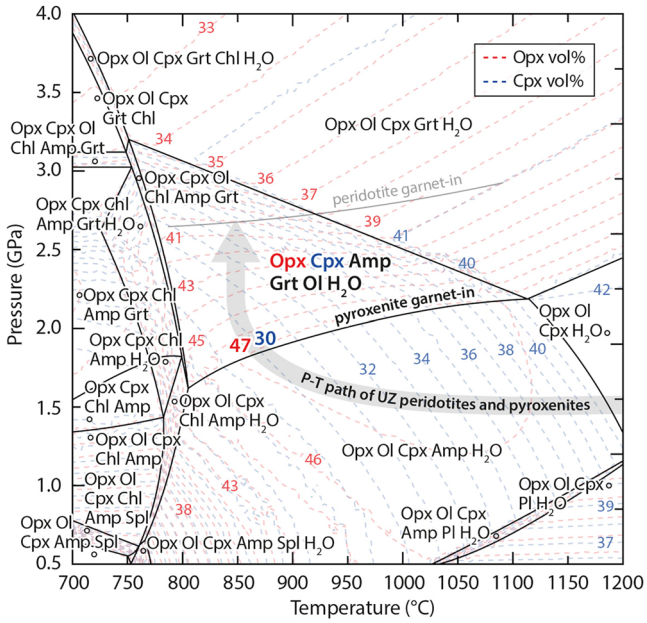

Figure 10. P-T isochemical section at H_2O saturated condition of the garnet websterite UT23 (composition in wt%: Na_2O = 0.60, MgO = 23.91, Al_2O_3 = 5.93, SiO_2 = 50.62, K_2O = 0.06, CaO = 9.94, and FeO = 5.35; a detailed description of the working conditions during inductively-coupled plasma mass spectrometry (ICP-MS) and LECO combustion (total C, S) analyses is given in Text S2 of Supporting Information S1). The compositions of Opx, Cpx, Grt, and Amp calculated from thermodynamic modeling are reported in Table S3. Thin dashed red and blue lines represent the isopleths of orthopyroxene and clinopyroxene volume fractions (vol%), respectively. The thin gray line is the garnet-in curve of UZ peridotites from Nimis and Morten (2000). The thick transparent gray line is the P-T path of UZ pyroxenites and peridotites (Nimis and Morten, 2000).

where σ_{diff} is the differential stress in MPa and d is the grain size in μm.

The flow law of Dimanov and Dresen (2005) has been used to calculate the contribution of dislocation creep and diffusion creep to the total strain rate for clinopyroxene:

$$\dot{\varepsilon} = A_{gss}\ \sigma^{n_{gss}}\ d^{-m}\ e^{-\frac{Q_{gss}}{RT}} + A_{gsi}\ \sigma^{n_{gsi}}\ e^{-\frac{Q_{gsi}}{RT}} \quad (4)$$

where $\dot{\varepsilon}$ is the strain rate (s^{-1}), A is the pre-exponential constant (given in $Pa^{-n}s^{-1}$ for GSI creep and $Pa^{-n}s^{-1}m^3$ for GSS creep; see caption of Table S2), σ is the differential stress (Pa), n is the stress exponent, d is the grain size (m), m is the grain size exponent, Q is the activation energy ($Jmol^{-1}$), R is the molar gas constant ($JK^{-1}mol^{-1}$), and T is the absolute temperature (K). The subscripts *gss* and *gsi* indicate the grain-size sensitive (diffusion creep) and the grain-size insensitive (dislocation creep) components of the total strain rate $\dot{\varepsilon}$. All the parameters used for calculation of deformation mechanism maps are given in Table S2 of supporting information.

Microstructures and crystallographic orientation data suggest that the transition from dislocation to diffusion creep in garnet websterites was promoted by the transformation of the coarse-grained Opx_P and Cpx_P into the finer grained Opx_N and Cpx_N. The switch in the deformation mechanism and the reduction of the grain size were also accompanied by the crystallization of garnet as exsolutions in high-T pyroxene porphyroclasts and as neoblasts in textural equilibrium with the finer grained Cpx_N + Opx_N + Amp_N matrix, indicating that deformation probably took place at high-pressure (HP) conditions.

To better constrain the P-T conditions at which deformation occurred, we calculated a P-T isochemical section (Figure 10) using the composition of garnet websterite UT23 (caption of Figure 10). Results indicate that the Cpx_N + Opx_N + Amp_N + Grt_N assemblage observed in the recrystallized matrix of garnet websterites is thermodynamically stable at pressure from 1.5 to 3.0 GPa and temperature ranging from 750 °C to 1100 °C (Figure 10). Following the prograde P-T path of the ultramafic rocks of the UZ reported in Figure 10 (Nimis & Morten, 2000), the Cpx_N + Opx_N + Amp_N + Grt_N assemblage is expected to form at ca. 2 GPa and 850 °C. Therefore, the shift from porphyroclastic to neoblastic assemblage and the switch in the deformation mechanism are interpreted to have occurred when garnet websterites, after a stage of isobaric cooling, crossed the garnet-in reaction curve at ca. 2 GPa and 850 °C (Figure 10) prior to be dragged to greater depths at nearly constant temperature. Also, at these conditions, garnet websterites are expected to be composed by 47 vol% of orthopyroxene and 30 vol% of clinopyroxene (Figure 10).

Thus, to describe the deformational behavior of the investigated garnet websterites, flow laws and deformation mechanism maps have been calculated at the peak temperature of 850°C. Many petrological studies also suggest that at these conditions, metamorphism in the UZ was accompanied by intense fluid infiltration (Tumiati et al., 2003, 2007). This is consistent with our observation of amphibole (Amp_N) in association with Cpx_N + Opx_N + Grt_N, indicating that recrystallization and deformation occurred in the presence of H_2O. Despite this, the occurrence of amphibole in the recrystallized matrix does not unequivocally imply the presence of intracrystalline H_2O in Cpx_N and Opx_N. To fully describe the deformational behavior of our garnet websterites, we therefore calculated flow laws and deformation mechanism maps for both dry and wet conditions. As no flow laws are available for wet orthopyroxene, we investigated the rheology of the garnet websterites using the flow laws for dry orthopyroxene (Bruijn & Skemer, 2014; Bystricky et al., 2016) and for dry and wet clinopyroxene (Dimanov & Dresen, 2005).

In Figure 9a, a differential stress of 15 MPa was estimated from the subgrain size of Opx_P (57.5 μm). Assuming that the differential stress is representative of the bulk flow stress, deformation by dislocation creep in Opx_P would occur at strain rates of 3.8×10^{-16} s^{-1} (Figure 9a). For the calculated σ_{diff} = 15 MPa, the Opx_N is expected

to flow at strain rates of 2.9×10^{-16} s^{-1}. In the grain size versus differential stress diagram of Figure 9a, these values (yellow star) plot close to the boundary between dislocation creep and diffusion creep. Also, we note that the average grain size of Opx_N is slightly larger than the subgrain size. We attribute this to partial annealing and grain growth of Opx_N, yet this grain size plots close to the transition between the different deformation regimes. It is likely that grain growth and annealing were limited by the syn-kinematic nucleation of second phases, which kept the grain size sufficiently small for the local activity of diffusion creep.

Figure 9b and 9c describe the rheological behavior of Cpx_N. For the range of differential stress estimated from the subgrain size in Opx_N, at dry conditions, the Cpx_N would deform via diffusion creep at strain rates of 4.4×10^{-15} s^{-1}, which are one order of magnitude faster than the strain rates calculated for Opx_N (Figure 9b). Faster strain rates of 3.15×10^{-12} s^{-1} have been calculated using the flow law for wet clinopyroxene (Figure 9c), which might be more appropriate in our case considering that the finding of amphibole in association with Cpx_N + Opx_N + Grt_N suggests the presence of a free fluid phase at the grain boundaries. In addition, the relative proportions of Opx_N (47 vol%) and Cpx_N (30 vol%) estimated by thermodynamic model of Figure 10 and the microstructural evidence of the presence of interconnected layers of Cpx_N through the garnet websterite (Figure 3a) indicate that the bulk deformation of garnet websterites would be controlled by the strength of the weaker phase between Opx_N and Cpx_N (e.g., Handy, 1990). Cpx_N is the weakest phase, since it is expected to flow at faster strain rates than Opx_N both under dry and wet conditions (Figure 9d), thus likely being responsible for rheological weakening of investigated websterites.

5.3. The Role of Pyroxenites in Mantle Weakening

Pyroxenites are important constituents of the upper mantle, and despite their low volumetric abundance, they represent key lithologies in mantle deformation processes since compositional heterogeneities can play a major role in strain localization and weakening (e.g., Tommasi et al., 2015; Tikoff et al., 2010; Toy et al., 2010; Treagus & Sokoutis, 1992).

The origin of pyroxenites has been related to a variety of magmatic and metamorphic processes, including: i) recycling of crustal material during subduction (Allègre & Turcotte, 1986; Kornprobst et al., 1990; Morishita & Arai, 2001; Morishita et al., 2003; Yu et al., 2010); ii) moderate- to high-pressure crystal segregation from magmas rising from asthenospheric mantle sources (Bodinier et al., 1987a, 1987b; Dantas et al., 2007; Gysi et al., 2011; Kempton & Stephens, 1997; Keshav et al., 2007; Mukasa & Shervais, 1999; Rivalenti et al., 1995; Takazawa et al., 1999; Vannucci et al., 1993; Warren et al., 2009); iii) refertilization of "depleted" upper mantle through melt-peridotite reactions during asthenospheric upwelling (Bodinier et al., 2008; Dantas et al., 2009; Garrido & Bodinier, 1999; Van Acken et al., 2010); and iv) reaction between peridotites and fluids/melts derived by high-pressure dehydration/melting of the subducted crust (e.g. Malaspina et al., 2006, 2017; Pellegrino et al., 2020; Wang et al., 2008).

Pyroxenites occur ubiquitously in most of oceanic and orogenic peridotite massifs, such as Lherz in the Pyrenees, Beni Bousera and Ronda in the Betic-Rif belt, Lanzo, Erro-Tobbio, Monte Duria, and Ulten Zone in the Alps (Bodinier et al., 2008; Dickey, 1970; Frets et al., 2012; Garrido and Bodinier, 1999; Gysi et al., 2011; Kornprobst, 1969, 1970; Morten & Obata, 1983; Rampone & Borghini, 2008; Tumiati et al., 2018). The studied pyroxenites occurring in the UZ have been interpreted as crystal segregation from a basaltic melt rising from the deeper portions of the mantle wedge (Nimis and Morten, 2000). These pyroxenites record a mineral phase transformation from coarse-grained websterites to finer grained garnet websterites (Morten and Obata, 1983; Nimis and Morten, 2000). Host peridotites record a similar evolution from coarse protogranular spinel lherzolites to fine-grained amphibole + garnet peridotites (Obata and Morten, 1987). This coupled evolution has been interpreted to reflect pressure increase and cooling of websterites and host peridotites from spinel- (1200 °C, 1.3−1.6 GPa) to garnet-facies (850 °C and 2.7 GPa) conditions induced by mantle corner flow (Nimis and Morten, 2000).

Microstructures indicate that the re-equilibration of garnet websterites in the garnet stability field was accompanied by a strong reduction of the grain size with the consequent switch of the deformation mechanism from dislocation creep in the porphyroclasts to diffusion creep in the finer grained neoblasts, resulting in rheological weakening. However, grain-size reduction could be not sufficient to cause a permanent transition from dislocation to diffusion creep because of grain growth (De Bresser et al., 2001), unless the latter is inhibited by other processes such as metamorphic reactions (e.g., Newman et al., 1999). In the investigated samples, the reduction

of the grain size was assisted by the crystallization of garnet in response to the re-equilibration of garnet websterites in the garnet stability field. In particular, garnet exsolved from coarse-grained pyroxenes contributing to the reduction of the grain size through the progressive disruption of the porphyroclastic assemblage and crystallized along the garnet websterite foliation, facilitating the pinning of the recrystallized matrix and stabilizing the fine-grained microtexture for diffusion creep and rheological weakening.

It is demonstrated that syn-deformational metamorphic reactions, such as the breakdown of a mantle aluminous phase (plagioclase, spinel, and garnet), can promote a switch to diffusion creep and the associated weakening in the upper mantle (e.g., Furusho & Kanagawa, 1999; Newman et al., 1999). The stability of these aluminous phases is strongly affected by major elements composition and at fixed P-T conditions, pyroxenites and peridotites can develop different phase assemblages as a result of different compositions (e.g. Schmädicke, 2000). Numerous experimental studies have also demonstrated that garnet forms at lower pressures in pyroxenites with respect to peridotites (e.g., Adam et al., 1992; Borghini & Fumagalli, 2018; Irving, 1974). Therefore, during the prograde path of UZ mantle rocks toward the slab-mantle interface, the reduction of the grain size, the switch in the deformation mechanism, and the rheological weakening associated with the transition from spinel- to garnet-facies conditions would occur at shallower depths in websterites compared to the host peridotite. This indicates that compositional variations (for example, the occurrence of pyroxenites) may also represent rheological heterogeneities where weakening and deformation can localize, thus suggesting that the distribution and the degree of deformation in the upper mantle may be strongly controlled by the presence and the volumetric fraction of compositional heterogeneities such as websterites.

Similar processes have also been documented by Hidas et al. (2013) in the Ronda Peridotite massif. The authors showed that the rheological weakening of thin pyroxenite layers was associated with a decrease of the grain size and an increase of the volume fraction of plagioclase in response to the spinel-plagioclase phase transformation reaction. This process induces the activation of GSS creep mechanisms and the rheological weakening of the pyroxenite bands that also affects the host peridotite. Our study demonstrates that reaction weakening can occur not only during the exhumation of the subcontinental mantle, but also during its burial toward the slab interface in response to the corner flow.

The schematic illustration of Figure 11 reports a conceptual model for the weakening of garnet websterites during the mantle corner flow. At high temperature and low pressure (1 in Figure 11), spinel lherzolites are intruded by melts rising from the deeper portions of the wedge, leading to the formation of coarse-grained websterites (Morten & Obata, 1983) characterized by large, high-T, tschermakitic pyroxenes (c.f. Table S3 and Nimis & Morten, 2000). Mantle convection (solid gray lines in Figure 11) induced by the movement of the subducting plate causes cooling and pressure increase of websterites while moving toward the slab-mantle interface (path from 1 to 2 in Figure 11). Cooling and pressure increase induce the solid-state exsolution of garnet by removing the Tschermak component from the coarse, high-T, tschermakitic pyroxenes (Gasparik, 1990; Spengler et al., 2012), and the crystallization of garnet along the websterite foliation. At this stage, syn-kinematic exsolution reactions are accompanied by dislocation creep and dynamic recrystallization of pyroxene porphyroclasts. This produces a reduction of the grain size, triggering a transition in deformation mechanism from dislocation creep to diffusion creep. The associated weakening of garnet websterites likely created favorable conditions for the incorporation of garnet websterites and host peridotites into the subducting crust.

6. Conclusions

The re-equilibration of websterites of UZ in the garnet stability field occurred under a deformation regime. Microstructures, EBSD data, and TEM investigations suggest that orthopyroxene porphyroclasts dominantly deformed by recrystallization-accommodated dislocation creep on the (100)[010] slip system, while the recrystallized pyroxene grains record deformation by dominant diffusion-accommodated grain boundary sliding.

Thermodynamic modeling indicates that the transition from dislocation creep to diffusion creep likely took place at 2 GPa and 850 °C during the prograde re-equilibration of websterites in the garnet stability field. During the cooling from 1200 to 850 °C, the Al-rich porphyroclastic pyroxenes exsolved garnet along the cleavages, which progressively crystallized forming the garnet websterite foliation, then triggering the pinning of the recrystallized matrix and stabilizing the fine-grained microtexture for diffusion creep. The activation of the diffusion creep induced a significant rheological weakening in the garnet websterites that also affected the host peridotite, thus

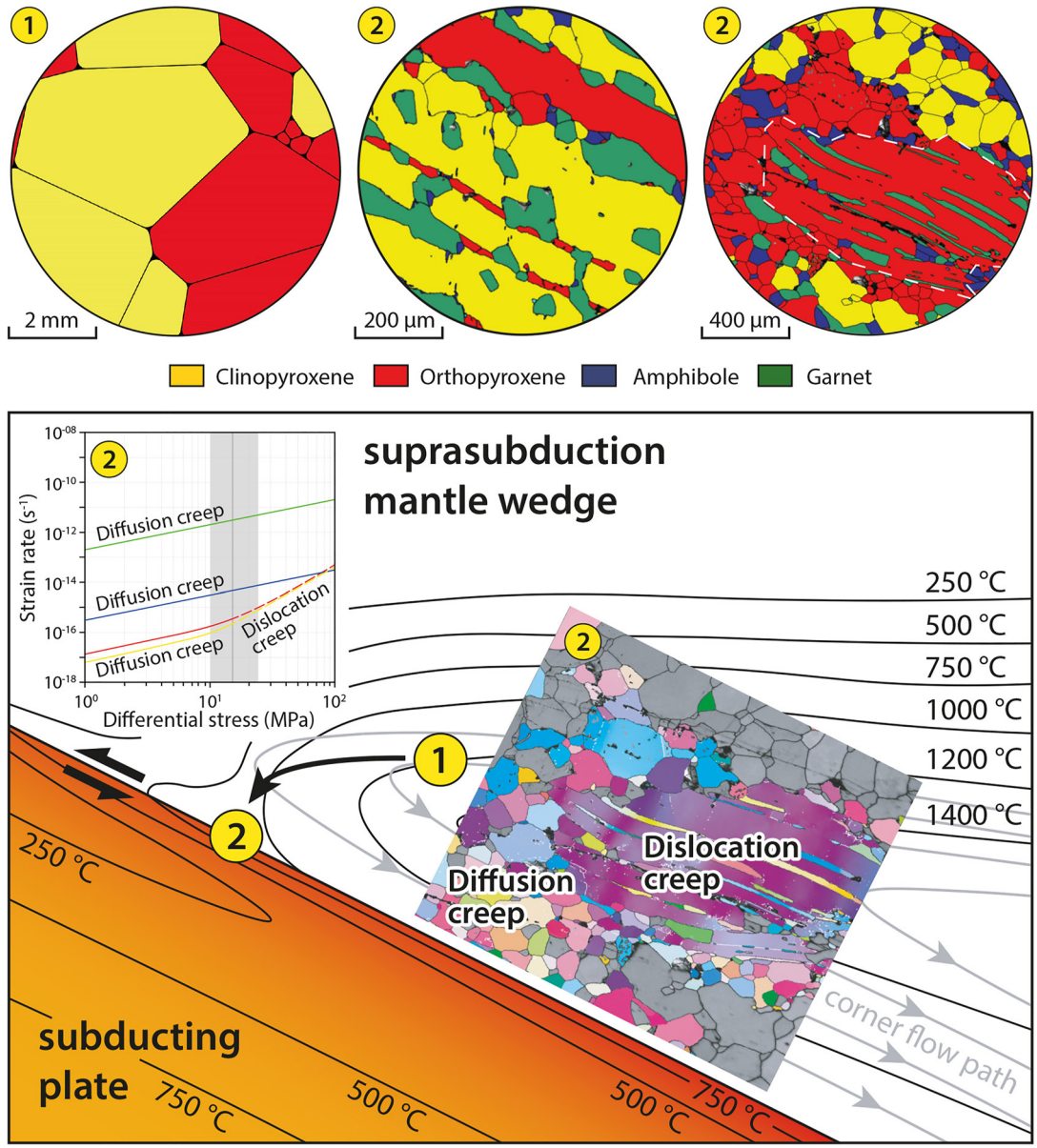

Figure 11. Conceptual model for mantle weakening induced by mantle corner flow (not to scale). See text for explanation. Model thermal configuration after Honda (1985). Black bold line represents metamorphic path of garnet websterites of UZ. Solid gray lines represent mantle corner flow path.

suggesting that the occurrence of compositional heterogeneities, e.g., pyroxenites l.s., can have important effect on the bulk rheological behavior of the upper mantle.

Conflict of Interest

The authors declare no conflicts of interest relevant to this study.

Data Availability Statement

The supporting information and the data set for this study can be found at https://doi.org/10.17632/shvnp5hdp4.2

Acknowledgments
The staff of the University of Plymouth Electron Microscopy Centre is thanked for assistance during EBSD data acquisition. We also thank A. Risplendente for the support during electron microprobe analyses. This work was funded by the Italian Ministry of University and Research (PRIN 2017—Prot. 2017ZE49E7_005—The Dynamic Mass Transfer from Slabs to Arcs—Dynastars and MIUR-DAAD Joint Mobility Program—The redox state of the Earth's mantle: from the slab-mantle interface to the sub-continental lithosphere). This work also benefited from Erasmus Plus Traineeship program. F.L. is grateful to the Deutsche Forschungsgemeinschaft for funding the TEM facilities via the Gottfried-Wilhelm-Leibniz programme (LA830/14-1). M. Campione is thanked for stimulating discussions and A. Ceccato for help with rheological calculations and EBSD data postprocessing with Channel5. We thank Luiz Morales and Jolien Linckens for their constructive reviews that have significantly improved the manuscript.

References

Adam, J., Green, T. H., & Day, R. A. (1992). An experimental study of two garnet pyroxenite xenoliths from the Bullenmerri and Gnotuk Maars of western Victoria, Australia. *Contributions to Mineralogy and Petrology*, *111*(4), 505–514. https://doi.org/10.1007/BF00320905

Allègre, C. J., & Turcotte, D. L. (1986). Implications of a two-component marble-cake mantle. *Nature*, *323*(6084), 123–127. https://doi.org/10.1038/323123a0

Ashby, M. F., & Verrall, R. A. (1973). Diffusion-accommodated flow and superplasticity. *Acta metallurgica*, *21*(2), 149–163. https://doi.org/10.1016/0001-6160(73)90057-6

Bachmann, F., Hielscher, R., & Schaeben, H. (2010). Texture Analysis with MTEX-Free and Open Source Software Toolbox. *Solid State Phenomena*, *160*, 63–68. https://doi.org/10.4028/www.scientific.net/SSP.160.63

Bai, Q., & Kohlstedt, D. L. (1992). High-temperature creep of olivine single crystals III. Mechanical results for unbuffered samples and creep mechanisms. *Philosophical Magazine A*, *66*(6), 1149–1181. https://doi.org/10.1080/01418619208248011

Bestmann, M., & Prior, D. J. (2003). Intragranular dynamic recrystallization in naturally deformed calcite marble: diffusion accommodated grain boundary sliding as a result of subgrain rotation recrystallization. *Journal of Structural Geology*, *25*(10), 1597–1613. https://doi.org/10.1016/S0191-8141(03)00006-3

Bodinier, J. L., Fabriès, J., Lorand, J. P., Dostal, J., & Dupuy, C. (1987a). Geochemistry of amphibole pyroxenite veins from the Lherz and Freychinede ultramafic bodies (Ariege, French Pyrenees). *Bulletin de minéralogie*, *110*(4), 345–358. https://doi.org/10.3406/bulmi.1987.8032

Bodinier, J. L., Garrido, C. J., Chanefo, I., Bruguier, O., & Gervilla, F. (2008). Origin of pyroxenite–peridotite veined mantle by refertilization reactions: evidence from the Ronda peridotite (Southern Spain). *Journal of Petrology*, *49*(5), 999–1025. https://doi.org/10.1093/petrology/egn014

Bodinier, J. L., Guiraud, M., Fabries, J., Dostal, J., & Dupuy, C. (1987). Petrogenesis of layered pyroxenites from the Lherz, Freychinede and Prades ultramafic bodies (Ariege, French Pyrenees). *Geochimica et Cosmochimica Acta*, *51*(2), 279–290. https://doi.org/10.1016/0016-7037(87)90240-7

Borghini, G., & Fumagalli, P. (2018). Subsolidus phase relations in a mantle pyroxenite: an experimental study from 0.7 to 1.5 GPa. *European Journal of Mineralogy*, *30*(2), 333–348. https://doi.org/10.1127/ejm/2018/0030-2735

Borghini, G., Fumagalli, P., & Rampone, E. (2010). The stability of plagioclase in the upper mantle: subsolidus experiments on fertile and depleted lherzolite. *Journal of Petrology*, *51*(1–2), 229–254. https://doi.org/10.1093/petrology/egp079

Boullier, A. M., & Gueguen, Y. (1975). SP-mylonites: origin of some mylonites by superplastic flow. *Contributions to Mineralogy and Petrology*, *50*(2), 93–104. https://doi.org/10.1007/BF00373329

Bürgmann, R., & Dresen, G. (2008). Rheology of the lower crust and upper mantle: Evidence from rock mechanics, geodesy, and field observations. *Annual Review of Earth and Planetary Sciences*, *36*, 531–567. https://doi.org/10.1146/annurev.earth.36.031207.124326

Braga, R., Massonne, H. J., & Morten, L. (2007). An early metamorphic stage for the Variscan Ulten Zone gneiss (NE Italy): Evidence from mineral inclusions in kyanite. *Mineralogical Magazine*, *71*(6), 691–702. https://doi.org/10.1180/minmag.2007.071.6.691

Braga, R., & Sapienza, G. T. (2007). The retrograde evolution of a dolomite-bearing hydrous peridotite from the Ulten Zone (Italian Alps). *GeoActa*, *6*, 37–45.

Bruijn, R. H., & Skemer, P. (2014). Grain-size sensitive rheology of orthopyroxene. *Geophysical Research Letters*, *41*(14), 4894–4903. https://doi.org/10.1002/2014GL060607

Bystricky, M., Lawlis, J., Mackwell, S., Heidelbach, F., & Raterron, P. (2016). High-temperature deformation of enstatite aggregates. *Journal of Geophysical Research: Solid Earth*, *121*(9), 6384–6400. https://doi.org/10.1002/2016JB013011

Christensen, N. I., & Lundquist, S. M. (1982). Pyroxene orientation within the upper mantle. *Geological Society of America BulletinCO*, *93*(4), 2792–288. https://doi.org/10.1130/0016-7606(1982)93<279:powtum>2.0.co;2

Connolly, J. A. (2005). Computation of phase equilibria by linear programming: a tool for geodynamic modeling and its application to subduction zone decarbonation. *Earth and Planetary Science Letters*, *236*(1-2), 524–541. https://doi.org/10.1016/j.epsl.2005.04.033

Dale, J., Holland, T., Powell, R. (2000). Hornblende–garnet–plagioclase thermobarometry: A natural assemblage calibration of the thermodynamics of hornblende. *Contributions to Mineralogy and Petrology*, *140*(3), 353–362. https://doi.org/10.1007/s004100000187

Dantas, C., Ceuleneer, G., Gregoire, M., Python, M., Freydier, R., Warren, J., & Dick, H. J. B. (2007). Pyroxenites from the Southwest Indian Ridge, 9–16 E: Cumulates from incremental melt fractions produced at the top of a cold melting regime. *Journal of Petrology*, *48*(4), 647–660. https://doi.org/10.1093/petrology/egl076

Dantas, C., Grégoire, M., Koester, E., Conceição, R. V., & Rieck, N., Jr. (2009). The lherzolite–websterite xenolith suite from Northern Patagonia (Argentina): Evidence of mantle–melt reaction processes. *Lithos*, *107*(1-2), 107–120. https://doi.org/10.1016/j.lithos.2008.06.012

De Bresser, J., Ter Heege, J., & Spiers, C. (2001). Grain size reduction by dynamic recrystallization: Can it result in major rheological weakening? *International Journal of Earth Sciences*, *90*(1), 28–45. https://doi.org/10.1007/s005310000149

Del Moro, A., Martin, S., & Prosser, G. (1999). Migmatites of the Ulten Zone (NE Italy), a record of melt transfer in deep crust. *Journal of Petrology*, *40*(12), 1803–1826. https://doi.org/10.1093/petroj/40.12.1803

Demouchy, S., Schneider, S. E., Mackwell, S. J., Zimmerman, M. E., & Kohlstedt, D. L. (2009). Experimental deformation of olivine single crystals at lithospheric temperatures. *Geophysical Research Letters*, *36*(4). https://doi.org/10.1029/2008GL036611

Dickey, J. S. (1970). *Partial fusion products in alpine peridotites: Serrania de la Ronda and other examples* (Vol. 3, pp. 33–49). Mineralogical Society of America Special Paper.

Dimanov, A., & Dresen, G. (2005). Rheology of synthetic anorthite-diopside aggregates: Implications for ductile shear zones. *Journal of Geophysical Research: Solid Earth*, *110*(B7). https://doi.org/10.1029/2004JB003431

Doukhan, N., Doukhan, J. C., Fitz Gerald, J. D., Chopra, P. N., & Paterson, M. S. (1984). A Tem Microstructural Study of Experimentally Deformed Anita Bay Dunite. In R.E. Tressler, & R.C. Bradt (Eds.), *Deformation of Ceramic Materials II. Materials Science Research* (Vol. 18, pp. 307–319). Springer. https://doi.org/10.1007/978-1-4615-6802-5_20

Drury, M. R., Vissers, R. L., Van der Wal, D., & Strating, E. H. H. (1991). Shear localisation in upper mantle peridotites. *Pure and Applied Geophysics*, *137*(4), 439–460. https://doi.org/10.1007/BF00879044

Durham, W. B., & Goetze, C. (1977). Plastic flow of oriented single crystals of olivine: 1. Mechanical data. *Journal of geophysical Research*, *82*(36), 5737–5753. https://doi.org/10.1029/JB082i036p05737

Durham, W. B., Goetze, C., & Blake, B. (1977). Plastic flow of oriented single crystals of olivine: 2. Observations and interpretations of the dislocation structures. *Journal of Geophysical Research*, *82*(36), 5755–5770. https://doi.org/10.1029/JB082i036p05755

Frets, E., Tommasi, A., Garrido, C. J., Padrón-Navarta, J. A., Amri, I., & Targuisti, K. (2012). Deformation processes and rheology of pyroxenites under lithospheric mantle conditions. *Journal of Structural Geology*, *39*, 138–157. https://doi.org/10.1016/j.jsg.2012.02.019

Fumagalli, P., & Poli, S. (2005). Experimentally determined phase relations in hydrous peridotites to 6· 5 GPa and their consequences on the dynamics of subduction zones. *Journal of Petrology*, *46*(3), 555–578. https://doi.org/10.1093/petrology/egh088

Furusho, M., & Kanagawa, K. (1999). Transformation-induced strain localization in a lherzolite mylonite from the Hidaka metamorphic belt of central Hokkaido, Japan. *Tectonophysics*, *313*(4), 411–432. https://doi.org/10.1016/S0040-1951(99)00215-2

Garrido, C. J., & Bodinier, J. L. (1999). Diversity of mafic rocks in the Ronda peridotite: evidence for pervasive melt-rock reaction during heating of subcontinental lithosphere by upwelling asthenosphere. *Journal of petrology*, *40*(5), 729–754. https://doi.org/10.1093/petroj/40.5.729

Gasparik, T. (1990). Phase relations in the transition zone. *Journal of Geophysical Research: Solid Earth*, *95*(B10), 15751–15769. https://doi.org/10.1029/JB095iB10p15751

Gebauer, D., & Grünenfelder, M. (1978). U-Pb dating of alpine-type garnet-peridotites example: Val Ultimo (Eastern Alps, northern Italy). U. S. Geol. Surv. Open-File Report. *OF*, *78–0701*, 135–137.

Godard, G., & Martin, S., (2000). Petrogenesis of kelyphites in garnet peridotites: A case study from the Ulten zone, Italian Alps. *Journal of Geodynamics*, *30*(1-2), 117–145. https://doi.org/10.1016/S0264-3707(99)00030-7

Godard, G., Martin, S., Prosser, G., Kienast, J. R., & Morten, L. (1996). Variscan migmatites, eclogites and garnet-peridotites of the Ulten zone, Eastern Austroalpine system. *Tectonophysics*, *259*(4), 313–341. https://doi.org/10.1016/0040-1951(95)00145-X

Gysi, A. P., Jagoutz, O., Schmidt, M. W., & Targuisti, K. (2011). Petrogenesis of pyroxenites and melt infiltrations in the ultramafic complex of Beni Bousera, Northern Morocco. *Journal of Petrology*, *52*(9), 1679–1735. https://doi.org/10.1093/petrology/egr026

Handy, M. R. (1989). Deformation regimes and the rheological evolution of fault zones in the lithosphere: The effects of pressure, temperature, grainsize and time. *Tectonophysics*, *163*(1–2), 119–152. https://doi.org/10.1016/0040-1951(89)90122-4

Handy, M. R. (1990). The solid-state flow of polymineralic rocks. *Journal of Geophysical Research: Solid Earth*, *95*(B6), 8647–8661. https://doi.org/10.1029/JB095iB06p08647

Hansen, L. N., Zimmerman, M. E., & Kohlstedt, D. L. (2011). Grain boundary sliding in San Carlos olivine: Flow law parameters and crystallographic-preferred orientation. *Journal of Geophysical Research: Solid Earth*, *116*(B8). https://doi.org/10.1029/2011JB008220

Hauzenberger, C. A., Höller, W., & Hoinkes, G. (1996). Transition from eclogite to amphibolite-facies metamorphism in the Austroalpine Ulten Zone. *Mineralogy and Petrology*, *58*(3–4), 111–130. https://doi.org/10.1007/BF01172092

Herzberg, C., Riccio, L., Chiesa, S., Fornoni, A., Gatto, G. O., Gregnanin, A., & Piccirillo, E. M. (1977). Petrogenetic evolution of the spinel–garnet-lherzolite in the Austridic crystalline basement from Val Clapa (Alto Adige, northeastern Italy). *Memorie dell'Istituto di Geologia, Universita` di Padova*, *30*, 3–28.

Hidas, K., Garrido, C. J., Tommasi, A., Padrón-Navarta, J. A., Thielmann, M., Konc, Z., & Marchesi, C. (2013). Strain localization in pyroxenite by reaction-enhanced softening in the shallow subcontinental lithospheric mantle. *Journal of Petrology*, *54*(10), 1997–2031. https://doi.org/10.1093/petrology/egt039

Hielscher, R., & Schaeben, H. (2008). A novel pole figure inversion method: specification of the MTEX algorithm. *Journal of Applied Crystallography*, *41*(6), 1024–1037. https://doi.org/10.1107/S0021889808030112

Hirth, G., & Kohlstedf, D. (2003). Rheology of the upper mantle and the mantle wedge: A view from the experimentalists. *Geophysical Monograph-American Geophysical Union*, *138*, 83–105. https://doi.org/10.1029/138GM06

Hoinkes, G., & Thöni, M. (1993). Evolution of the Ötztal-Stubai, Scarl-Campo and Ulten basement units. In J.F. von Raumer, & F. Neubauer (Eds.), *Pre-mesozoic geology in the Alps* (pp. 485–494). Springer. https://doi.org/10.1007/978-3-642-84640-3_29

Holland, T., & Powell, R. (2003). Activity-composition relations for phases in petrological calculations: An asymmetric multicomponent formulation. *Contributions to Mineralogy and Petrology*, *145*(4), 492–501. https://doi.org/10.1007/s00410-003-0464-z

Holland, T. J. B., & Powell, R. T. J. B. (1998). An internally consistent thermodynamic data set for phases of petrological interest. *Journal of metamorphic Geology*, *16*(3), 309–343. https://doi.org/10.1111/j.1525-1314.1998.00140.x

Honda, S. (1985). Thermal structure beneath Tohoku, northeast Japan. *Tectonophysics*, *112*(1–4), 69–102. https://doi.org/10.1016/0040-1951(85)90173-8

Irving, A. J. (1974). Geochemical and high pressure experimental studies of garnet pyroxenite and pyroxene granulite xenoliths from the Delegate basaltic pipes, Australia. *Journal of Petrology*, *15*(1), 1–40. https://doi.org/10.1093/petrology/15.1.1

Ishii, K., & Sawaguchi, T. (2002). Lattice-and shape-preferred orientation of orthopyroxene porphyroclasts in peridotites: An application of two-dimensional numerical modeling. *Journal of Structural Geology*, *24*(3), 517–530. https://doi.org/10.1016/S0191-8141(01)00078-5

Jahn, S., & Martoňák, R. (2008). Plastic deformation of orthoenstatite and the ortho-to high-pressure clinoenstatite transition: A metadynamics simulation study. *Physics and Chemistry of Minerals*, *35*(1), 17–23. https://doi.org/10.1007/s00269-007-0194-2

Jaroslow, G. E., Hirth, G., & Dick, H. J. B. (1996). Abyssal peridotite mylonites: Implications for grain-size sensitive flow and strain localization in the oceanic lithosphere. *Tectonophysics*, *256*(1–4), 17–37. https://doi.org/10.1016/0040-1951(95)00163-8

Jung, H., Katayama, I., Jiang, Z., Hiraga, T., & Karato, S. I. (2006). Effect of water and stress on the lattice-preferred orientation of olivine. *Tectonophysics*, *421*(1–2), 1–22. https://doi.org/10.1016/j.tecto.2006.02.011

Jung, H., Park, M., Jung, S., & Lee, J. (2010). Lattice preferred orientation, water content, and seismic anisotropy of orthopyroxene. *Journal of Earth Science*, *21*(5), 555–568. https://doi.org/10.1007/s12583-010-0118-9

Kaczmarek, M. A., & Tommasi, A. (2011). Anatomy of an extensional shear zone in the mantle, Lanzo massif, Italy. *Geochemistry, Geophysics, Geosystems*, *12*(8), a–n. https://doi.org/10.1029/2011GC003627

Kempton, P. D., & Stephens, C. J. (1997). Petrology and geochemistry of nodular websterite inclusions in harzburgite, Hole 920D. In J.A. Karson, M. Cannat, D.J. Miller, & D. Elthon (Eds.), *Proceedings of the Ocean Drilling Program, Scientific Results* (Vol. 153, pp. 321–331). Texas A&M University Digital Library. https://doi.org/10.2973/odp.proc.sr.153.030.1997

Keshav, S., Sen, G., & Presnall, D. C. (2007). Garnet-bearing xenoliths from Salt Lake Crater, Oahu, Hawaii: High-pressure fractional crystallization in the oceanic mantle. *Journal of Petrology*, *48*(9), 1681–1724. https://doi.org/10.1093/petrology/egm035

Kohlstedt, D. L., & Vander Sande, J. B. (1973). Transmission electron microscopy investigation of the defect microstructure of four natural orthopyroxenes. *Contributions to Mineralogy and Petrology*, *42*(2), 169-180. https://doi.org/10.1007/BF00371506

Kornprobst, J. (1969). Le massif ultrabasique des Beni Bouchera (Rif Interne, Maroc): Etude des péridotites de haute température et de haute pression, et des pyroxénolites, à grenat ou sans grenat, qui leur sont associées. *Contributions to Mineralogy and Petrology*, *23*(4), 283–322. https://doi.org/10.1007/BF00371425

Kornprobst, J. (1970). Les péridotites et les pyroxénolites du massif ultrabasique des Beni Bouchera: Une étude expérimentale entre 1100 et 1550° C, sous 15 à 30 kilobars de pression sèche. *Contributions to Mineralogy and Petrology*, *29*(4), 290–309. https://doi.org/10.1007/BF00371277

Kornprobst, J., Piboule, M., Roden, M., & Tabit, A. (1990). Corundum-bearing garnet clinopyroxenites at Beni Bousera (Morocco): Original plagioclase-rich gabbros recrystallized at depth within the mantle? *Journal of Petrology*, *31*(3), 717–745. https://doi.org/10.1093/petrology/31.3.717

Lavina, B., Carbonin, S., Russo, U., & Tumiati, S. (2006). The crystal structure of dissakisite-(La) and structural variations after annealing of radiation damage. *American Mineralogist*, *91*(1), 104–110. https://doi.org/10.2138/am.2006.1721

Linckens, J., Bruijn, R. H., & Skemer, P. (2014). Dynamic recrystallization and phase mixing in experimentally deformed peridotite. *Earth and Planetary Science Letters*, *388*, 134–142. https://doi.org/10.1016/j.epsl.2013.11.037

Linckens, J., Herwegh, M., Müntener, O., & Mercolli, I. (2011). Evolution of a polymineralic mantle shear zone and the role of second phases in the localization of deformation. *Journal of Geophysical Research: Solid Earth*, *116*(B6). https://doi.org/10.1016/j.jsg.2011.08.011

Mainprice, D., Barruol, G., & Ismail, W. B. (2000). The Seismic Anisotropy of the Earth's Mantle from Single Crystal to Polycrystal. *Geophysical Monograph*, *117*, 237–264. https://doi.org/10.1029/GM117p0237

Malaspina, N., Hermann, J., Scambelluri, M., & Compagnoni, R. (2006). Polyphase inclusions in garnet–orthopyroxenite (Dabie Shan, China) as monitors for metasomatism and fluid-related trace element transfer in subduction zone peridotite. *Earth and Planetary Science Letters*, *249*(3-4), 173–187. https://doi.org/10.1016/j.epsl.2006.07.017

Malaspina, N., Langenhorst, F., Tumiati, S., Campione, M., Frezzotti, M. L., & Poli, S. (2017). The Redox Budget of Crust-Derived Fluid Phases at the Slab-Mantle Interface. *Geochimica et Cosmochimica Acta*, *209*, 70–84. https://doi.org/10.1016/j.gca.2017.04.004

Malaspina, N., & Tumiati, S. (2012). The role of COH and oxygen fugacity in subduction-zone garnet peridotites. *European Journal of Mineralogy*, *24*(4), 607–618. https://doi.org/10.1127/0935-1221/2012/0024-2213

Marocchi, M., Hermann, J., Tropper, P., Bargossi, G. M., & Mair, V. (2010). Amphibole and phlogopite in "hybrid" metasomatic bands monitor trace element transfer at the interface between felsic and ultramafic rocks (Eastern Alps, Italy). *Lithos*, *117*(1-4), 135–148. https://doi.org/10.1016/j.lithos.2010.02.011

Marocchi, M., Mair, V., Tropper, P., & Bargossi, G. M. (2009). Metasomatic reaction bands at the Mt. Hochwart gneiss-peridotite contact (Ulten Zone, Italy): Insights into fluid-rock interaction in subduction zones. *Mineralogy and Petrology*, *95*(3-4), 251–272. https://doi.org/10.1007/s00710-009-0043-8

Maruyama, G., & Hiraga, T. (2017). Grain-to multiple-grain-scale deformation processes during diffusion creep of forsterite + diopside aggregate: 1. Direct observations. *Journal of Geophysical Research: Solid Earth*, *122*(8), 5890–5915. https://doi.org/10.1002/2017JB014254

Martin, S., Godard, G., Prosser, G., Schiavo, A., Bernoulli, D., & Ranalli, G. (1998). Evolution of the deep crust at the junction Austroalpine/Southalpine: The Tonale Nappe. *Memorie di Scienze Geologiche*, *50*, 3–50.

Martin, S., Morten, L., & Prosser, G. (1993). Metamorphic and structural evolution of the Spl- to Grt-peridotites and surrounding basement rocks from the Nonsberg area. In L. Morten (Ed.), *Italian Eclogites and Related Rocks* (Vol. 13, pp. 237–251). Accademia Nazionale delle Scienze detta dei XL.Roma.

Miranda, E. A., Hirth, G., & John, B. E. (2016). Microstructural evidence for the transition from dislocation creep to dislocation-accommodated grain boundary sliding in naturally deformed plagioclase. *Journal of Structural Geology*, *92*, 30–45. https://doi.org/10.1016/j.jsg.2016.09.002

Morishita, T., & Arai, S. (2001). Petrogenesis of corundum-bearing mafic rock in the Horoman Peridotite Complex, Japan. *Journal of Petrology*, *42*(7), 1279–1299. https://doi.org/10.1093/petrology/42.7.1279

Morishita, T., Arai, S., Gervilla, F., & Green, D. H. (2003). Closed-system geochemical recycling of crustal materials in alpine-type peridotite. *Geochimica et Cosmochimica Acta*, *67*(2), 303–310. https://doi.org/10.1016/S0016-7037(02)01079-7

Morten, L., & Obata, M. (1983). Possible high-temperature origin of pyroxenite lenses within garnet peridotite, northern Italy. *Bulletin de minéralogie*, *106*(6), 775–780. https://doi.org/10.3406/bulmi.1983.7699

Morten, L., & Trommsdorff, V. (2003). Metamorphism and textures of dry and hydrous garnet peridotites. In D.A. Carswell, & R. Compagnoni (Eds.), *Ultrahigh Pressure Metamorphism, EMU Notes in Mineral*ogy (Vol. 5, pp. 443–46). Eotvos University Press.Budapest.

Mukasa, S. B., & Shervais, J. W. (1999). Growth of subcontinental lithosphere: evidence from repeated dike injections in the Balmuccia lherzolite massif, Italian Alps. *Lithos*, *48*(1–4), 287–316. https://doi.org/10.1016/S0024-4937(99)00033-X

Nazé, L., Doukhan, N., Doukhan, J. C., & Latrous, K. (1987). A TEM study of lattice defects in naturally and experimentally deformed orthopyroxenes. *Bulletin de minéralogie*, *110*(5), 497–512. https://doi.org/10.3406/bulmi.1987.7993

Newman, J., Lamb, W. M., Drury, M. R., & Vissers, R. L. (1999). Deformation processes in a peridotite shear zone: Reaction-softening by an H_2O-deficient, continuous net transfer reaction. *Tectonophysics*, *303*(1–4), 193–222. https://doi.org/10.1016/S0040-1951(98)00259-5

Nimis, P., & Morten, L. (2000). P-T evolution of 'crustal' garnet peridotites and included pyroxenites from Nonsberg area (upper Austroalpine), NE Italy: From the wedge to the slab. *Journal of Geodynamics*, *30*(1–2), 93–115. https://doi.org/10.1016/S0264-3707(99)00029-0

Obata, M., & Morten, L. (1987). Transformation of spinel lherzolite to garnet lherzolite in ultramafic lenses of the Austridic crystalline complex, northern Italy. *Journal of Petrology*, *28*(3), 599–623. https://doi.org/10.1093/petrology/28.3.599

Pellegrino, L., Malaspina, N., Zanchetta, S., Langone, A., & Tumiati, S. (2020). High pressure melting of eclogites and metasomatism of garnet peridotites from Monte Duria Area (Central Alps, N Italy): A proxy for melt-rock reaction during subduction. *Lithos*, *358–359*, 105391. https://doi.org/10.1016/j.lithos.2020.105391

Précigout, J., Gueydan, F., Gapais, D., Garrido, C. J., & Essaifi, A. (2007). Strain localisation in the subcontinental mantle—a ductile alternative to the brittle mantle. *Tectonophysics*, *445*(3–4), 318–336. https://doi.org/10.1016/j.tecto.2007.09.002

Prior, D. J., Wheeler, J., Peruzzo, L., Spiess, R., & Storey, C. (2002). Some garnet microstructures: an illustration of the potential of orientation maps and misorientation analysis in microstructural studies. *Journal of Structural Geology*, *24*(6-7), 999–1011. https://doi.org/10.1016/S0191-8141(01)00087-6

Raleigh, C. B., Kirby, S. H., Carter, N. L., & Lallemant, H. A. (1971). Slip and the clinoenstatite transformation as competing rate processes in enstatite. *Journal of Geophysical Research*, *76*(17), 4011–4022. https://doi.org/10.1029/JB076i017p04011

Rampone, E., & Borghini, G. (2008). Melt migration and intrusion in the Erro-Tobbio peridotites (Ligurian Alps, Italy): Insights on magmatic processes in extending lithospheric mantle. *European Journal of Mineralogy*, *20*(4), 573–585. https://doi.org/10.1127/0935-1221/2008/0020-1807

Rampone, E., & Morten, L. (2001). Records of crustal metasomatism in the garnet peridotites of the Ulten Zone (Upper Austroalpine, Eastern Alps). *Journal of Petrology*, *42*(1), 207–219. https://doi.org/10.1093/petrology/42.1.207

Ranalli, G., Martin, S., & Mahatsente, R. (2005). Continental subduction and exhumation: an example from the Ulten Unit, Tonale Nappe, Eastern Austroalpine. *Geological Society, London, Special Publications*, *243*(1), 159–174. https://doi.org/10.1144/gsl.sp.2005.243.01.12

Rivalenti, G., Mazzucchelli, M., Vannucci, R., Hofmann, A. W., Ottolini, L., Bottazzi, P., & Obermiller, W. (1995). The relationship between websterite and peridotite in the Balmuccia peridotite massif (NW Italy) as revealed by trace element variations in clinopyroxene. *Contributions to Mineralogy and Petrology*, *121*(3), 275–288. https://doi.org/10.1007/BF02688243

Rutter, E. H., & Brodie, K. H. (1988). The role of tectonic grain size reduction in the rheological stratification of the lithosphere. *Geologische Rundschau*, *77*(1), 295–307. https://doi.org/10.1007/BF01848691

Sapienza, G. T., Scambelluri, M., & Braga, R. (2009). Dolomite-bearing orogenic garnet peridotites witness fluid-mediated carbon recycling in a mantle wedge (Ulten Zone, Eastern Alps, Italy). *Contributions to Mineralogy and Petrology*, *158*(3), 401–420. https://doi.org/10.1007/s00410-009-0389-2

Scambelluri, M., Hermann, J., Morten, L., & Rampone, E. (2006). Melt-versus fluid-induced metasomatism in spinel to garnet wedge peridotites (Ulten Zone, Eastern Italian Alps): Clues from trace element and Li abundances. *Contributions to Mineralogy and Petrology*, *151*(4), 372–394. https://doi.org/10.1007/s00410-006-0064-9

Scambelluri, M., Rampone, E., Braga, R., & Malaspina, N. (2010). The Variscan garnet peridotites from the Eastern Alps (Ulten Zone): Records of subduction metasomatism in the mantle wedge. *Journal of the Virtual Explorer*. In Marco Beltrando, Angelo Peccerillo, Massimo Mattei, Sandro Conticelli, and Carlo Doglioni. The Geology of Italy (Vol. *36*). https://doi.org/10.3809/jvirtex.2010.00259

Schmädicke, E. (2000). Phase relations in peridotitic and pyroxenitic rocks in the model systems CMASH and NCMASH. *Journal of Petrology*, *41*(1), 69–86. https://doi.org/10.1093/petrology/41.1.69

Skemer, P., Katayama, I., & Karato, S. I. (2006). Deformation fabrics of the Cima di Gagnone peridotite massif, Central Alps, Switzerland: Evidence of deformation at low temperatures in the presence of water. *Contributions to Mineralogy and Petrology*, *152*(1), 43–51. https://doi.org/10.1007/s00410-006-0093-4

Skemer, P., Warren, J. M., Kelemen, P. B., & Hirth, G. (2010). Microstructural and rheological evolution of a mantle shear zone. *Journal of Petrology*, *51*(1–2), 43–53. https://doi.org/10.1093/petrology/egp057

Skrotzki, W. (1994). Defect structure and deformation mechanisms in naturally deformed augite and enstatite. *Tectonophysics*, *229*(1–2), 43–68. https://doi.org/10.1016/0040-1951(94)90005-1

Skrotzki, W., Wedel, A., Weber, K., & Müller, W. F. (1990). Microstructure and texture in lherzolites of the Balmuccia massif and their significance regarding the thermomechanical history. *Tectonophysics*, *179*(3-4), 227–251. https://doi.org/10.1016/0040-1951(90)90292-G

Soustelle, V., Tommasi, A., Demouchy, S., & Ionov, D. A. (2010). Deformation and fluid–rock interaction in the supra-subduction mantle: Microstructures and water contents in peridotite xenoliths from the Avacha Volcano, Kamchatka. *Journal of Petrology*, *51*(1–2), 363–394. https://doi.org/10.1093/petrology/egp085

Spengler, D., Obata, M., Hirajima, T., Ottolini, L., Ohfuji, H., Tamura, A., & Arai, S. (2012). Exsolution of garnet and clinopyroxene from high-Al pyroxenes in Xugou peridotite, Eastern China. *Journal of Petrology*, *53*(7), 1477–1504. https://doi.org/10.1093/petrology/egs023

Susini, S., & Martin, S. (1996). Microstrutture nelle peridotiti della serie d'Ultimo (Austroalpino superiore, Alpi orientali). *Atti Ticinesi di Scienze della Terra*, *4*, 47–63.

Svahnberg, H., & Piazolo, S. (2010). The initiation of strain localisation in plagioclase-rich rocks: Insights from detailed microstructural analyses. *Journal of Structural Geology*, *32*(10), 1404–1416. https://doi.org/10.1016/j.jsg.2010.06.011

Takazawa, E., Frey, F. A., Shimizu, N., Saal, A., & Obata, M. (1999). Polybaric petrogenesis of mafic layers in the Horoman peridotite complex, Japan. *Journal of Petrology*, *40*(12), 1827–1851. https://doi.org/10.1093/petroj/40.12.1827

Tikoff, B., Larson, C. E., Newman, J., & Little, T. (2010). Field-based constraints on finite strain and rheology of the lithospheric mantle, Twin Sisters Washington *Lithosphere*, *2*(6), 418–422. https://doi.org/10.1130/L97.1

Tommasi, A., & Vauchez, A. (2015). Heterogeneity and anisotropy in the lithospheric mantle. *Tectonophysics*, *661*, 11–37. https://doi.org/10.1016/j.tecto.2015.07.026

Tommasi, A., Vauchez, A., & Ionov, D. A. (2008). Deformation, static recrystallization, and reactive melt transport in shallow subcontinental mantle xenoliths (Tok Cenozoic volcanic field, SE Siberia). *Earth and Planetary Science Letters*, *272*(1–2), 65–77. https://doi.org/10.1016/j.epsl.2008.04.020

Toy, V. G., Newman, J., Lamb, W., & Tikoff, B. (2010). The role of pyroxenites in formation of shear instabilities in the mantle: Evidence from an ultramafic ultramylonite, Twin Sisters Massif, Washington. *Journal of Petrology*, *51*(1–2), 55–80. https://doi.org/10.1093/petrology/egp059

Treagus, S. H., & Sokoutis, D. (1992). Laboratory modelling of strain variation across rheological boundaries. *Journal of Structural Geology*, *14*(4), 405–424. https://doi.org/10.1016/0191-8141(92)90102-3

Tumiati, S., Godard, G., Martin, S., Klötzli, U., & Monticelli, D. (2007). Fluid-controlled crustal metasomatism within a high-pressure subducted mélange (Mt. Hochwart, Eastern Italian Alps). *Lithos*, *94*(1–4), 148–167. https://doi.org/10.1016/j.lithos.2006.06.009

Tumiati, S., Godard, G., Martin, S., Nimis, P., Mair, V., & Boyer, B. (2005). Dissakisite-(La) from the Ulten zone peridotite (Italian Eastern Alps): A new end-member of the epidote group. *American Mineralogist*, *90*(7), 1177–1185. https://doi.org/10.2138/am.2005.1710

Tumiati, S., & Martin, S. (2003). Garnet-peridotite in the Italian Eastern Alps: 150 years of discoveries. *Memorie di Scienze Geologiche dell'Università di Padova*, *55*, 31–46.

Tumiati, S., Thöni, M., Nimis, P., Martin, S., & Mair, V. (2003). Mantle-crust interactions during Variscan subduction in the Eastern Alps (Nonsberg–Ulten zone): geochronology and new petrological constraints. *Earth and Planetary Science Letters*, *210*(3–4), 509–526. https://doi.org/10.1016/S0012-821X(03)00161-4

Tumiati, S., Zanchetta, S., Pellegrino, L., Ferrario, C., Casartelli, S., & Malaspina, N. (2018). Granulite-facies overprint in garnet peridotites and kyanite eclogites of Monte Duria (Central Alps, Italy): Clues from srilankite-and sapphirine-bearing symplectites. *Journal of Petrology*, *59*(1), 115–151. https://doi.org/10.1093/petrology/egy021

Van Acken, D., Becker, H., Walker, R. J., McDonough, W. F., Wombacher, F., Ash, R. D., & Piccoli, P. M. (2010). Formation of pyroxenite layers in the Totalp ultramafic massif (Swiss Alps)–insights from highly siderophile elements and Os isotopes. *Geochimica et Cosmochimica Acta*, *74*(2), 661–683. https://doi.org/10.1016/j.gca.2009.10.007

Van Duysen, J. C., Doukhan, N., & Doukhan, J. C. (1985). Transmission electron microscope study of dislocations in orthopyroxene (Mg, Fe)$_2$Si$_2$O$_6$. *Physics and Chemistry of Minerals*, *12*(1), 39–44. https://doi.org/10.1007/BF00348745

Vannucci, R., Shimizu, N., Piccardo, G. B., Ottolini, L., & Bottazzi, P. (1993). Distribution of trace elements during breakdown of mantle garnet: an example from Zabargad. *Contributions to Mineralogy and Petrology*, *113*(4), 437–449. https://doi.org/10.1007/BF00698314

Vauchez, A., & Garrido, C. J. (2001). Seismic properties of an asthenospherized lithospheric mantle: constraints from lattice preferred orientations in peridotite from the Ronda massif. *Earth and Planetary Science Letters*, *192*(2), 235–249. https://doi.org/10.1016/S0012-821X(01)00448-4

Vauchez, A., Tommasi, A., & Mainprice, D. (2012). Faults (shear zones) in the Earth's mantle. *Tectonophysics*, *558*, 1–27. https://doi.org/10.1016/j.tecto.2012.06.006

Wang, J., Hattori, K. H., & Stern, C. R. (2008). Metasomatic origin of garnet orthopyroxenites in the subcontinental lithospheric mantle underlying Pali Aike volcanic field, southern South America. *Mineralogy and Petrology*, *94*(3–4), 243–258. https://doi.org/10.1007/s00710-008-0017-2

Warren, J. M., & Hirth, G. (2006). Grain size sensitive deformation mechanisms in naturally deformed peridotites. *Earth and Planetary Science Letters*, *248*(1–2), 438–450. https://doi.org/10.1016/j.epsl.2006.06.006

Warren, J. M., Shimizu, N., Sakaguchi, C., Dick, H. J. B., & Nakamura, E. (2009). An assessment of upper mantle heterogeneity based on abyssal peridotite isotopic compositions. *Journal of Geophysical Research: Solid Earth*, *114*(B12). https://doi.org/10.1029/2008JB006186

Wheeler, J., Prior, D., Jiang, Z., Spiess, R., & Trimby, P. (2001). The petrological significance of misorientations between grains. *Contributions to mineralogy and petrology*, *141*(1), 109–124. https://doi.org/10.1007/s004100000225

White, S. (1977). Geological significance of recovery and recrystallization processes in quartz. *Tectonophysics*, *39*(1–3), 143–170. https://doi.org/10.1016/0040-1951(77)90093-2

White, S. (1979). Grain and sub-grain size variations across a mylonite zone. *Contributions to Mineralogy and Petrology*, *70*(2), 193–202. https://doi.org/10.1007/BF00374448

White, S. H., Burrows, S. E., Carreras, J., Shaw, N. D., & Humphreys, F. J. (1980). On mylonites in ductile shear zones. *Journal of Structural Geology*, *2*(1–2), 175–187. https://doi.org/10.1016/0191-8141(80)90048-6

Whitney, D. L., & Evans, B. W. (2010). Abbreviations for names of rock-forming minerals. *American mineralogist*, *95*(1), 185-187. https://doi.org/10.2138/am.2010.3371

Xu, Z., Wang, Q., Ji, S., Chen, J., Zeng, L., Yang, J., & Wenk, H. R. (2006). Petrofabrics and seismic properties of garnet peridotite from the UHP Sulu terrane (China): implications for olivine deformation mechanism in a cold and dry subducting continental slab. *Tectonophysics*, *421*(1–2), 111–127. https://doi.org/10.1016/j.tecto.2006.04.010

Yu, S. Y., Xu, Y. G., Ma, J. L., Zheng, Y. F., Kuang, Y. S., Hong, L. B. & Tong, L.-X. (2010). Remnants of oceanic lower crust in the subcontinental lithospheric mantle: trace element and Sr–Nd–O isotope evidence from aluminous garnet pyroxenite xenoliths from Jiaohe, Northeast China. *Earth and Planetary Science Letters*, *297*(3–4), 413–422. https://doi.org/10.1016/j.epsl.2010.06.043

Ziberna, L., Klemme, S., & Nimis, P. (2013). Garnet and spinel in fertile and depleted mantle: Insights from thermodynamic modelling. *Contributions to Mineralogy and Petrology*, *166*(2), 411–421. https://doi.org/10.1007/s00410-013-0882-5